Université Libre de Bruxelles

Faculté des Sciences – Département de Physique

Louis Moureaux

Étude de la production exclusive du méson ρ dans les données proton-plomb prises à CMS en 2013 à $\sqrt{s_{NN}} = 5.02\,\text{TeV}$

Directeur:
Laurent Favart

Année académique 2016-2017.

Mémoire présenté en vue de l'obtention
du diplôme de Master en Sciences Physiques.

Study of exclusive production of the ρ meson
in proton-lead data taken at CMS in 2013
at $\sqrt{s_{NN}} = 5.02\,\text{TeV}$

Résumé

Ce travail consiste en la mesure de la section efficace de photoproduction du méson ρ sur le proton à haute énergie dans le système du centre de masse. La mesure est effectué à partir des données proton-plomb du LHC prises en 2013 par le détecteur CMS.

Après introduction des éléments théoriques nécessaires et une description du dispositif expérimental, des coupures d'exclusivité sont définies afin de diminuer autant que possible la contribution des bruits de fond. La contribution résiduelle après sélection est estimée et soustraite du signal observé.

La dépendence de la section efficace de photoproduction du méson ρ en l'énergie dans le système du centre de masse est estimée, ainsi que la section efficace différentielle en t. Nos mesures sont en accord avec celles effectuées auprès d'autres expériences.

Mots-clefs : Physique des hautes énergies, LHC, CMS, photoproduction, collisions ultrapériphériques, section efficace.

Abstract

The goal of this work is to measure of the cross section for ρ meson photoproduction on proton targets, at high center-of-mass energy. The LHC proton-lead data taken by CMS in 2013 is used to perform the measurement.

After introducing the necessary theoretical elements and describing the experimental setup, exclusivity cuts are defined in order to lower as much as possible the background contribution. The residual contribution after the selection is estimated and subtracted from the observed signal.

The dependence of ρ meson photoproduction cross section on the center-of-mass energy is estimated, as well as the t-differential cross section. Our results are in agreement with those from other experiments.

Keywords: High-energy physics, LHC, CMS, photoproduction, ultraperipheral collisions, cross section.

Acknowledgments

First and foremost, I would like to thank Laurent Favart for the many hours he spent discussing with me. This work wouldn't have been possible without his patience and motivation.

The discussions I had with Pascal Vanlaer and Sefano Pironio triggered improvements to the analysis. Let me thank them for this, and wish them a pleasant reading.

I would like to thank the FSQ-16-007 authors, too, who kindly provided, among others, the Monte-Carlo simulations used in this work. Nothing would have been possible without their valuable input.

Last but not least, I would like to thank my family for their support, and the many problems they solved just by asking me to somehow vulgarize them.

Contents

Warning: This is a modified version, fixing some typos and unclear statements. The text as submitted to the jury can be obtained by mailing me (lmoureau@ulb.ac.be) or Laurent Favart (lfavart@ulb.ac.be).

Introduction

Quantum mechanics is a very successful theory. Three of the four fundamental interactions can be described using its combination with special relativity, the quantum theory of fields. Some of the most accurate predictions in physics involve relativistic quantum mechanics. Predictions of the theory were tested experimentally across more than ten orders of magnitude.

One the corner stones of quantum mechanics is the unitarity of time evolution. Since it plays a central role in our understanding of nature, any possible experimental deviation has to be investigated: proving quantum mechanics to be wrong would be a major discovery.

Today's measurements of the proton structure seem to challenge unitarity: it looks like the density of low-energy gluons grows without limit. If this turns out to be true, our description of physics is facing a major problem. Otherwise, understanding how unitarity kicks in is still a very interesting problem.

The low-energy (or low momentum fraction x) contents of the proton can only be probed in high-energy collisions. Small momentum fractions are probed by the production of light particles close to the beam pipe. Probing the small-x gluon density is thus acheived by studying the production of light resonances (i.e. below the Z mass).

The present work is in line with this experimental programme. We measure the photon-proton cross section for one of the lightest possible final states, a single ρ^0 meson. We use data taken by the CMS detector in proton-lead collisions, at a nucleon-nucleon center-of-mass energy of 5.02 TeV. Our work is a cross-check and possible improvement of a CMS analysis [1]. We will often refer to it as FSQ-16-007.

The general organization of this Master's thesis is as follows.

In the first chapter, we introduce the elements of theory needed to understand the motivation of our work. We will also describe existing experimental results and explain how a photon-proton cross section can be extracted from proton-lead events.

The second chapter is a description of the LHC and of the CMS detector. We will mainly stay focused on information needed in order to understand the next chapter, though we'll say a bit more than strictly necessary.

We will detail our event samples and selection in the third chapter. In particular, we will describe how we use the CMS detector to reject as much background as possible. Monte-Carlo event samples will be mentioned at the end of the chapter.

In the fourth and last chapter, we will finally compute the cross section for ρ meson photoproduction. We will need to estimate the background and

subtract it from the selected event sample. Our results will be compared to those from past experiments.

Chapter 1

Motivation and theoretical background

This first chapter covers the theoretical framework around our work. We will start by introducing the Standard Model of particle physics, then focus on states bound by the strong interaction. We will then move on to the particular process studied here: photoproduction of the ρ meson on proton targets. We will describe a prediction for its high-energy behavior, and quickly review existing experimental results. The last two sections will cover ultra-peripheral collisions and the use of Monte-Carlo simulations at particle physics experiments.

As usual in particle physics, we set $c = \hbar = 1$. With this definition, energies, momenta and masses all share the same unit; distance use its inverse. We will use the electronvolt eV, and in particular two of its multiples, the MeV and the GeV. The unit of energies, momenta and masses is the GeV; distances can be written in GeV^{-1}.

1.1 The Standard Model of particle physics

The Standard Model (SM) [2] is the best description of particle physics currently available. It is based on the quantum field theory (QFT), which unifies quantum mechanics and special relativity. The SM describes three interactions: electromagnetism, the weak force and the strong force; gravitation is currrently missing. The weak interaction manifests itself at higher energies than those considered here, and will be neglected in the following.

Most calculations in QFT are based on perturbation theory around small coupling constants. When this development converges, the SM can be seen as a set of "matter" fermions interacting through the exchange of "mediator" bosons (see figure 1.1). How to perform calculations when it doesn't is an open problem.

An important feature of QFT is that coupling constants are actually not constant. Their variations are functions of a scale whose value is not given by the theory. It is usually taken as one of the Lorentz-invariant energies in the process; distances are sometimes used as well.

After a short overview of QED and QCD, the theories behind electromagnetism and the strong interaction, we will describe the spectrum of a class of

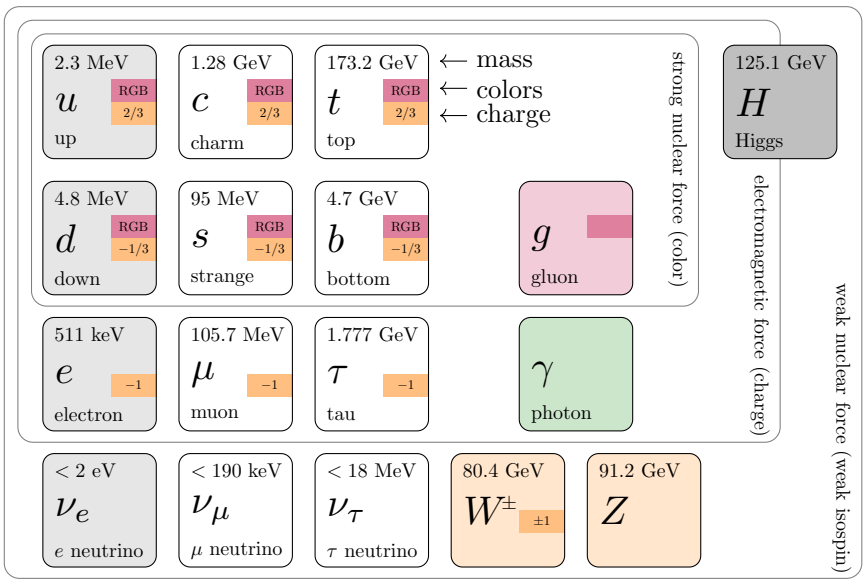

Figure 1.1: Particle contents of the Standard Model (adapted from [3]).

strongly bound particles, the mesons. An overview of the proton as a QCD bound state closes this section.

Quantum electrodynamics (QED)

QED was the first part of what's today called the Standard Model to be invented. It describes interactions between charged particles as the exchange of one or more "photons" (written γ). Many photons together make up a classical electromagnetic field obeying Maxwell's equations.

Just like light, photons are massless and have two polarizations; however, these constraints only apply to photons that can be observed ("real" or "on-shell" ones). "Virtual" photons can have any polarization and mass, but cannot travel far away.

The only free parameter of QED is the charge of the electron, which is usually chosen equal to one. In that case, the fine structure constant $\alpha \equiv e^2/4\pi$ is equal to $1/4\pi$. This constant increases slightly with the energy, and becomes infinite at a finite (huge) scale. We won't have to worry about those effects.

Quantum chromodynamics (QCD)

The strong interaction is more subtle than electrodynamics, and a satisfying description was only found in the seventies. QCD is based on particles called "quarks", with fractional electromagnetic charge. Each of these quarks comes in three "colors", and can interact with other color-charged particles by exchanging "gluons".

The main oddity of QCD is that the coupling constant is large at low energy, which prevents using perturbation theory below $\sim 1\,\text{GeV}$. The whole perturbative picture breaks down, and quarks and gluons are no more well-defined objects. In the presence of a "hard" scale (an energy whose value is

	Pseudoscalar		Vector	
Quark contents	Symbol	Mass	Symbol	Mass
$\frac{1}{\sqrt{2}}(u\bar{u} - d\bar{d})$	π^0	135	ρ^0	775
$u\bar{d}/\bar{u}d$	π^+/π^-	140	$\rho^\pm$	775
$u\bar{s}/\bar{u}s$	K^+/K^-	464	$K^{*\pm}$	892
$\bar{d}s/d\bar{s}$	$K^0/\bar{K}^0$	498	$K^{*0}/\bar{K}^{*0}$	896
$\frac{c_1}{\sqrt{2}}(u\bar{u} + d\bar{d}) + c_2(s\bar{s})$	η	548	ω	783
$\frac{c'_1}{\sqrt{2}}(u\bar{u} + d\bar{d}) + c'_2(s\bar{s})$	η'	958	ϕ	1 019

Table 1.1: Classification of light pseudoscalar and vector mesons [4]. Charge-conjugate particles are listed on the same line. Masses are in MeV.

bigger than a few GeV), the coupling constant is lower and perturbation theory may make sense – though it's not automatic.

Because the coupling constant is so strong (and increases with the distance between particles), colored states can't live for long: they immediately exchange gluons and eventually become color-neutral. This is the reason why quarks are always observed in bound, color-neutral states[1]. The lightest such states are made of two quarks; they are called mesons. Three-quarks bound states are called baryons; they include the proton and neutron.

The meson spectrum

Predicting the meson spectrum is hard because of the strong coupling constant. Fortunately, phenomenological arguments allow to understand it qualitatively.

Since the difference beween the up and down quarks masses is much smaller than the meson masses, swapping one for the other doesn't change much (as far as the strong interaction is concerned: they have different electric charges). If we allow arbitrary superpositions of u and d quarks, we end up with a representation of the su(2) algebra called Gell-Mann SU(2). More precisely, the (ud) doublet is in the $\mathbf{2}$ and $(\bar{u}\bar{d})$ is in the $\bar{\mathbf{2}}$.

Let's now construct mesons, using one quark and one antiquark. If the Gell-Mann symmetry holds, we end up doing $\mathbf{2} \otimes \bar{\mathbf{2}} = \mathbf{1} \oplus \mathbf{3}$: we get one particle in the representation $\mathbf{1}$, and three in the $\mathbf{3}$. Mesons in the same representation should have similar masses, because they end up mixing with each other when mixing the up and down quarks. The three particles in the $\mathbf{3}$ are called pions (symbol π), and the singlet η_8. The η_8 is actually not a mass eigenstate; we will see shortly that it mixes with another η.

The same argument using the three lightest quarks, u, d and s, leads to nine mesons, one in a singlet and all others in an octet (of su(3)). The octet contains the three pions, the $K^\pm$, the K^0 and $\bar{K}^0$, and the η_8. The singlet is called η_1. Because they share the same quantum numbers, the η_1 and η_8 mix with each other; the mass eigenstates are called η and η'.

So far, we only talked about mesons in their ground state, with spin 0 and negative parity ("pseudoscalar" ones). The first excited states have spin 1 and

[1] Apart from the top quark, which decays before having the time to form bound states.

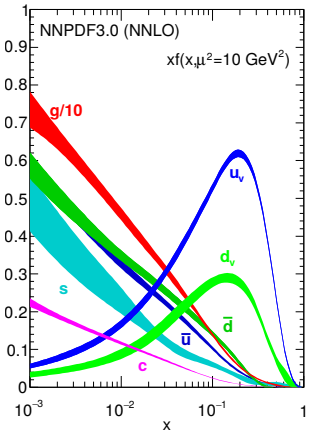

(a) Parton density functions (PDFs) evaluated at a scale $\mu^2 = 10\,\mathrm{GeV}^2$ [4].

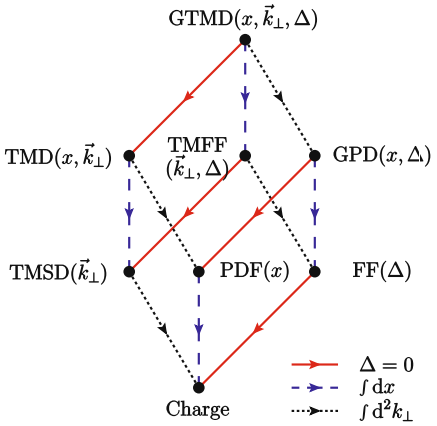

(b) Relations between TMDs, GPDs and related functions [6].

Figure 1.2: Parton density functions (left) and their generalizations (right). x is the momentum fraction of the produced parton; $\overrightarrow{k_\perp}$ is its transverse momentum; Δ is the four-momentum transferred at the proton vertex. TMFF stand for transverse momentum-dependant form factors, and TMSD for transverse momentum-dependant spin distributions.

negative parity, and are called "vector" mesons. Among them can be found the main topic of this work, the ρ^0, as well as the ω and ϕ, that will be important backgrounds. The Gell-Mann symmetry still holds; actually, its predictions are even better than in the scalar case.

Table 1.1 lists the lightest mesons and their quark contents. Apart from some trouble with the three pions (which can be explained by chiral symmetry breaking [5]), mesons in the same representation of su(3) have more or less the same mass. Variations inside the su(2) doublet are even smaller: the mass difference between the ρ^0 and the $\rho^\pm$ couldn't be measured to date [4].

The proton bound state

Protons (and neutrons) are baryons made of up and down quarks. Due to the strength of the strong coupling constant at low energy, their structure is in fact more complicated: along with their three "valence" quarks, protons contain gluons, and even other quarks (that make up the "sea"). The same is true for any hadron; these structures cannot be computed analytically.

The probability of finding a quark or gluon q in a proton is given by the parton density functions (PDF) $f_{q/p}(x;\mu^2)$, where μ^2 is a factorization scale and x is the momentum fraction carried by the parton [7]. The scale dependence of the PDFs is given by the DGLAP system of coupled differential equations. Recent values of the PDFs are shown of figure 1.2a.

The observed density of very low x gluons tends to be very high. It can't, however, go to infinity without breaking the unitarity of time evolution in quantum mechanics. The gluon density must therefore stop raising at some point (for example due to gluon recombination, $gg \to g$, not included in the DGLAP

equations because of unknown correlations in the gg initial state). This feature, called "gluon saturation", hasn't been observed so far in an unambiguous way.

Parton density functions are very useful, but they have a few important limitations. First, they only give a one-dimensional picture of the proton, which doesn't take transverse momentum into account. This problem can be solved by considering transverse momentum-dependant parton distributions (TMDs) [8]. Secondly, the relation between the PDFs and the proton form factors (FF) isn't clear; generalized parton distributions (GPDs) provide a natural unified framework. GPDs and TMDs are both specializations of even more general functions, called generalized TMDs (GTMDs). The relations between these functions are shown on figure 1.2b.

The main pitfall of TMDs and GPDs with respect to PDFs is their higher dimensionality: measuring them in the whole phase space is difficult. The first fits of TMDs to data appeared a few years ago; present research focuses on taking scale dependence into account. GPD fitting is more difficult because these functions have more parameters, but is also an active research area [9].

1.2 Vector meson (photo)production

The "golden channels" to access the GPDs (and in general the color distribution in the proton) are Compton scattering ($\gamma^* p \to \gamma p$) and exclusive meson production ($\gamma^* p \to Mp$) [10]. Both of them feature the same, well-understood initial state; the difference lies in the reaction products. From a theoretical point of view, predictions for exclusive meson production are more difficult because the connexion between perturbation theory and the meson final state is not fully understood. The two processes are in fact complementary because, as will be discussed below, they probe different GPDs.

Since it is the main topic here, we will focus on the production of vector mesons, $\gamma^* p \to Vp$. Conservation rules imply that the meson must be neutral, cannot carry strangeness/charm/bottomness, and must have negative parity. Many particles satisfy these conditions. Let's begin the list with the ρ and its two heavier versions, the $\rho(1450)$ and $\rho(1700)$ (hereafter referred to as ρ'). The ω and the ϕ are two other possible light mesons. Heavier ones, such as the J/ψ and $\psi(2s)$ ($c\bar{c}$ bound states) and the Υ ($b\bar{b}$), can also be produced. This list omits many rare resonances.

We can't go forward without first defining the kinematic variables describing the system. Once done, we'll describe three models for vector meson production. We will then present a prediction for the case of gluon saturation.

Kinematics

One of the most important variables is the virtuality of the incoming photon, $Q^2 = -q^2 > 0$, where q^μ is the photon four-momentum. We will develop the kinematics in the "photoproduction" domain (when $Q^2 \approx 0$); all Lorentz-invariant definitions remain valid in the "electroproduction" domain ($Q^2 > 0$). We use the following momentum assignments:

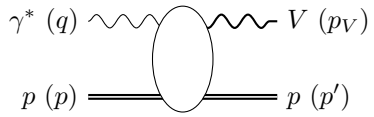

It is convenient to use a frame in which both the proton and photon momentums are along the z axis, and the proton is ultra-relativistic. Such a frame can always be defined, and we'll see later that it is close to the lab frame. In our frame, if the photon is real, one can take:

$$q^\mu = E_\gamma(1,0,0,1)^\mu \qquad \text{and} \qquad p^\mu = E_p(1,0,0,-1)^\mu,$$

where E_γ and E_p are respectively the photon and proton energies.

The final state momentums p_V and p' can be written as:

$$p_V^\mu = (E_V, \mathbf{p}_t, p_z^V)^\mu \qquad \text{and} \qquad p'^\mu = (E'_p, -\mathbf{p}_t, -p'_z)^\mu,$$

where $\mathbf{p}_t$ is the (two-dimensional) transverse momentum.

Two important Lorentz-invariant quantities are defined as follows: the photon-proton center-of-mass energy, W, is such that $W^2 \equiv (p+q)^2$; the square of the momentum transfer t is defined as $t \equiv (q - p_V)^2 = (p - p')^2$. Using four-momentum conservation and keeping only the leading power in E_p, we can write these variables as follows:

$$-t = p_t^2, \tag{1.1}$$

$$W^2 = 2E_p(E_V + p_z^V). \tag{1.2}$$

It is sometimes useful to consider the rapidity of the vector meson,

$$y_V \equiv \frac{1}{2}\log\frac{E_V + p_z^V}{E_V - p_z^V}.$$

At small p_t (with respect to the mass $M_V \equiv \sqrt{p_V^2}$ of the vector meson), equation (1.2) can be rewritten as $W = 2E_p M_V e^{y_V}$. We'll use the more precise version given by equation (1.2).

At high energy (of the vector meson with respect to its mass), the rapidity can be approximated by a purely geometrical variable, called pseudorapidity:

$$\eta_V \equiv \frac{1}{2}\log\frac{p_V + p_z^V}{p_V - p_z^V}.$$

Detector geometries are usually described in terms of η_V rather than the spherical polar angle θ_V.

Models for vector meson production

Several models have been proposed to describe exclusive vector meson production. We shortly discuss three of them in this section. We'll start with Vector Meson Dominance, an old but still relevant phenomenological model. We'll continue with a short overview of the color-dipole approach, a state-of-the-art predictive model. GPD-based computations will be examined last, with an emphasis on what vector meson production can teach us in this area.

Vector meson dominance

Vector meson dominance (VMD) [11] takes its roots in early attempts at describing the strong interaction. Today, it is considered as a phenomenological model. The principle is simple: the virtual photon is thought as a superposition of a purely electromagnetic state and a set of vector mesons with the same quantum numbers. In canonical VMD, only the lightest mesons (ω, ρ and ϕ) are included. Generalized versions include heavier resonances.

In the VMD picture for vector meson production, the photon first fluctuates into a vector meson, which then interacts with the proton. The case where the photon interacts before fluctuating is usually neglected, because electromagnetic coupling between the photon and the proton is much smaller than the strong coupling between the meson and the proton.

The first measured input of the model is the photon-meson coupling f_V, computed from the meson leptonic decay width, $\Gamma_{V\to e^+e^-}$:

$$\Gamma_{V\to e^+e^-} = \frac{4\pi\alpha}{f_V^2}\frac{M_V}{3},$$

where $\alpha = 1/4\pi$ is the fine structure constant. The leptonic decay width is a well-measured quantity [4].

Using this quantity, one writes the t-differential cross section $\mathrm{d}\sigma/\mathrm{d}t$ as:

$$\frac{\mathrm{d}\sigma_{\gamma p\to Vp}}{\mathrm{d}t} = \frac{e^2}{f_V^2}\frac{\mathrm{d}\sigma_{Vp\to Vp}}{\mathrm{d}t},$$

where $e = -1$ is the charge of the electron. This is in particular true at $t = 0$, in which case we can apply the optical theorem[2]:

$$\left.\frac{\mathrm{d}\sigma_{\gamma p\to Vp}}{\mathrm{d}t}\right|_{t=0} = \frac{e^2}{f_V^2}\frac{1+\beta^2}{16\pi}\,\sigma^2_{Vp\to X},$$

where β accounts for the contribution of the real part of the amplitude, that the optical theorem cannot predict.

The total inelastic cross section $\sigma_{Vp\to X}$ is parametrized as:

$$\sigma_{Vp\to X} = \sigma_M W^{-\eta} + \sigma_{\mathbb{P}} W^{\epsilon}. \tag{1.3}$$

The two terms are often referred to as coming from meson (σ_M) and "pomeron" ($\sigma_{\mathbb{P}}$) exchange.

The VDM doesn't predict the t differential cross-section; an exponential form is usually assumed:

$$\frac{\mathrm{d}\sigma_{\gamma p\to Vp}}{\mathrm{d}|t|} \propto e^{-b|t|}\sigma^2_{Vp\to X}. \tag{1.4}$$

[2] The optical theorem relates forward elastic scattering amplitudes to total cross sections. In our case, it reads:

$$\Im\mathcal{A}_{Vp\to Vp}\Big|_{t=0} = 4\pi\, W\, \sigma_{Vp\to X},$$

where $\sigma_{Vp\to X}$ is the total inelastic cross-section. It is an unavoidable consequence of the unitarity of time evolution in quantum mechanics; more details are found e.g. in chapter 24 of [2].

The parameter b above is called the t slope of the cross section. It is usually interpreted as the square of the transverse size of the interaction (i.e. including the proton, photon and vector meson sizes).

The VDM is valid for soft interactions (when QCD bound states interact as a whole and their composite nature is irrelevant). This is among others realized in high-energy photoproduction: $W \to \infty$ and $Q^2 \to 0$.

The color dipole model

The color dipole model [12, 13] is formulated in light-cone coordinates, with time being swapped for the $x^+ \equiv \frac{1}{\sqrt{2}}(x+t)$ coordinate. The basic idea is that the incoming photon fluctuates into a quark-antiquark pair, $\gamma^* \to q\bar{q}$, that forms a "color dipole". The dipole then interacts with the proton, and the projection of the result on the meson wave function gives the scattering amplitude.

More precisely, in terms of the vector meson and photon light-cone wave functions Ψ_V and Ψ, the imaginary part of the scattering amplitude can be written as:

$$\mathcal{A}_{\gamma p \to V p} = 2i \int \frac{\mathrm{d}^2\mathbf{r}}{4\pi} \int \mathrm{d}^2\mathbf{b} \int_0^1 \mathrm{d}z \, (\Psi_V^* \Psi) \, e^{-i[\mathbf{b}-(1-z)\mathbf{r}]\boldsymbol{\Delta}} \, \mathcal{N},$$

where $\mathbf{r}$ is the dipole separation, $\mathbf{b}$ is the impact parameter, z is the fraction of the photon light-cone momentum carried by the quark, and Δ is the momentum transfer at the proton vertex, $t = \Delta^2$. A summation over spin and quark flavours u, d, s, c is implied in $(\Psi_V^* \Psi)$, called the "overlap" between Ψ and Ψ_V.

The photon light-cone wave function Ψ can be computed in pure QED. Its equivalent for the vector meson Ψ_V cannot, but the so-called "boosted gaussian" wave functions reproduce currently available data for 1 s and 2 s meson states.

The proton-dipole scattering amplitude $\mathcal{N}(x, \mathbf{r}, \boldsymbol{\Delta})$ (x is the Björken variable) depends on the spatial distribution of gluons inside the proton; at small dipole sizes, it can be computed in perturbation theory. Outside of the perturbative regime, several different parametrizations based on gaussian (spatial) gluon distributions reproduce currently available experimental data.

The expression above is defined in such a way that:

$$\frac{\mathrm{d}\sigma_{\gamma p \to V p}}{\mathrm{d}t} = \frac{1+\beta^2}{16\pi} \left| \mathcal{A}_{\gamma p \to V p} \right|^2,$$

where $\beta^2 \lesssim 15\,\%$ accounts for the missing real part of the amplitude. The t-dependence of the exclusive vector meson cross sections therefore depend on the details of the proton-dipole scattering cross-section. In particular, it depends on the color distribution in the transverse plane of the proton.

GPD-based computations

The interpretation of vector meson production in terms of GPDs is only possible in certain kinematic regions. GPD factorization was formally proven at large photon virtuality and center-of-mass energy, $Q^2 \to \infty$ and $W \to \infty$, with the Björken variable x kept fixed, and in the photon-proton center-of-mass frame

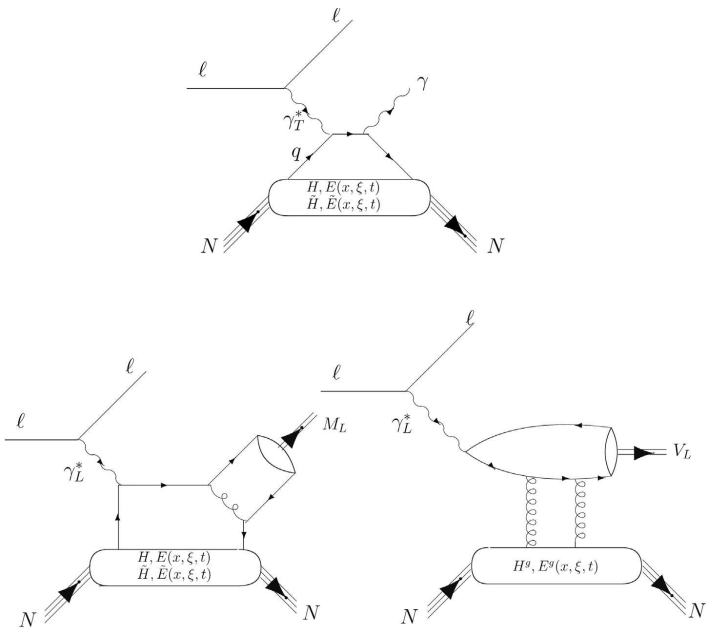

Figure 1.3: Typical diagrams of DVCS (top) and DVMP (bottom) using the GPDs E, $\tilde{E}$, H and $\tilde{H}$ [10]. The lepton ℓ can be swapped for any other charged particle. M_L stands for any vector or scalar meson, V_L for a vector meson.

[10]. Another proof was found for photoproduction (small Q^2) of $q\bar{q}$ mesons, in the formal limit $m_q \to \infty$.

Typical diagrams for deeply virtual ($Q^2 \to \infty$) Compton scattering (DVCS) and meson production (DVMP) are shown on figure 1.3. They show that, at leading order, DVCS depends only on the quark GPDs. DVMP depends on the GPDs for the quark species that make up the final state meson and, in the case of vector mesons, on the gluon GPDs. The latter contribution dominates at low x (for GPDs, x is defined with respect to the total exchanged momentum).

Unfortunately, ρ^0 photoproduction can't be interpreted in terms of the GPDs because the ρ is made of light quarks. Therefore, our analysis won't constrain generalized parton distributions.

A prediction for gluon saturation

A calculation [13] using the color dipole model indicates that gluon saturation could manifest itself through the appearance of a diffractive pattern in the $|t|$-differential vector meson cross sections (see figure 1.4). The differential cross section would feature several dips, which the authors claim is an universal feature of any gluon saturation model.

In the gluon saturation picture, the dips move to lower $|t|$ when increasing W or lowering the mass M_V of the considered meson. While dips could appear for other reasons, this is a distinctive feature of saturation models. Since the ρ is the lightest vector meson, gluon saturation could very well be first observed in ρ photoproduction.

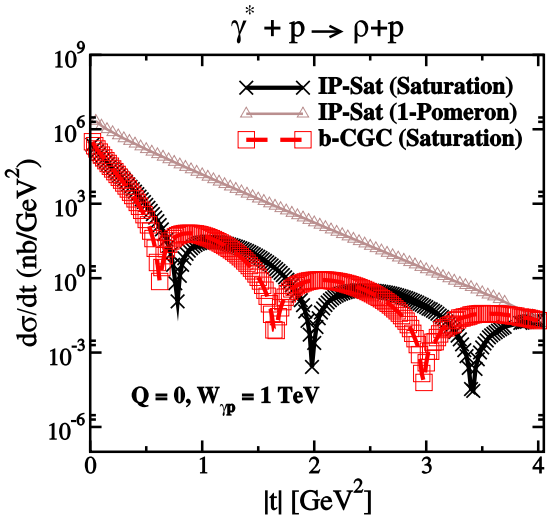

Figure 1.4: Diffractive pattern in the t-differential cross section for exclusive $\gamma p \to \rho p$ production in the gluon saturation picture [13]. This prediction was made for photoproduction at $W = 1\,\text{TeV}$; the red and black curves are two different models for gluon saturation, and the purple one is a model without saturation. Theoretical uncertainties are shown using the marker sizes.

If gluons saturate, the vector meson production cross sections are expected to saturate too. This would manifest itself by a deviation from the power law of the VDM at high W. The deviation in W predicted by [13] is, however, not significant at energies within reach of current data samples. Moreover, the results depend strongly on the quark masses, which aren't known with great accuracy.

1.3 Experimental results

Exclusive photoproduction of a ρ meson has been studied for a long time. Most of the available data lies below $W = 20\,\text{GeV}$; the two experiments that provided data above this threshold, H1 [14] and ZEUS [15], used the reaction $ep \to e\rho p$ at the HERA collider. The statistics used for their measurements at $Q^2 = 0$ were limited, because a special trigger configuration was needed in order to reach this domain. Precision measurements of exclusive ρ production on gold were recently performed using data taken at the Relativistic Heavy Ion Collider (RHIC) [16].

Mass peak and interference

The STAR collaboration at RHIC has recently been able to perform a precise measurement [16] of the various contributions to $\pi^+\pi^-$ production with $M_{\pi\pi}$ around $M_\rho = 775\,\text{MeV}$ in gold-gold collisions. The production mode is essentially the same as in our analysis, with the additional complication of the target being a nucleus. The photon-nucleon center-of-mass energy W is around 15 GeV.

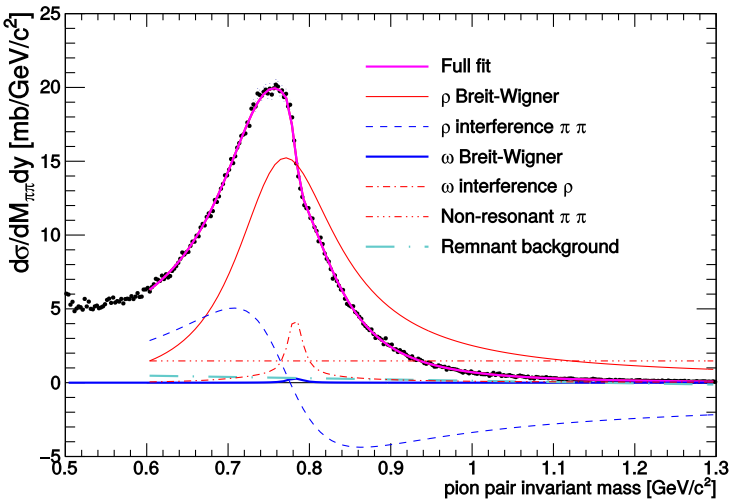

Figure 1.5: Contributions to the ρ mass peak, as measured by STAR [16].

Around the M_ρ, the amplitude $\mathcal{A}_{\pi\pi}$ for $\pi^+\pi^-$ production can be written as the sum of three terms [16],

$$\mathcal{A}_{\pi\pi} \propto A\frac{\sqrt{M_{\pi\pi}M_\rho\Gamma(M_{\pi\pi})}}{M_{\pi\pi}^2 - M_\rho^2 + iM_\rho\Gamma_\rho(M_{\pi\pi})} - B + Ce^{i\varphi}\frac{\sqrt{M_{\pi\pi}M_\omega\Gamma(M_{\pi\pi})}}{M_{\pi\pi}^2 - M_\omega^2 + iM_\omega\Gamma_\omega(M_{\pi\pi})},$$

where the first term describes ρ production, the second one direct $\pi^+\pi^-$ production and the last one stands for the ω.

In the expression above, all parameters are real and positive; $M_\omega = 783\,\text{MeV}$ is the mass of the ω. The variable widths Γ_ρ and Γ_ω take the variation of the available phase-space into account; for Γ_ρ, the expression is:

$$\Gamma_\rho(M_{\pi\pi}) = \Gamma_\rho^{\pi^+\pi^-}\frac{M_\rho}{M_{\pi\pi}}\left|\frac{M_{\pi\pi}^2 - 4m_\pi^2}{M_\rho^2 - 4m_\pi^2}\right|^{\frac{3}{2}}, \tag{1.5}$$

where $\Gamma_\rho^{\pi^+\pi^-} \approx \Gamma_\rho^{\text{tot}} = 149\,\text{MeV}$ is the partial decay width of the ρ into two charged pions, and $m_\pi = 140\,\text{MeV}$ is the mass of charged pions. A similar expression holds for $\Gamma_\omega(M_{\pi\pi})$; see [16] for details.

The STAR measurement shows that the three contributions are needed in order to describe the data (see figure 1.5). The most important part of the cross section comes from ρ production. The amplitudes for direct $\pi\pi$ and ω production are small, but their interferences with the ρ are important.

The effect of the ρ-$\pi\pi$ interference is to shift the apparent mass of the ρ to lower values, by increasing the cross section for $M_{\pi\pi} < M_\rho$ and lowering it above M_ρ. The ρ-ω interference term is much smaller, and only slightly changes the shape of the mass peak.

Most measurements of the ρ cross section neglect the contribution from the ω. In this case, the cross section is given by the Söding formula:

$$\frac{\mathrm{d}\sigma_{\gamma p\to\pi^+\pi^- }}{\mathrm{d}M_{\pi\pi}} = \left|A\frac{\sqrt{M_{\pi\pi}M_\rho\Gamma(M_{\pi\pi})}}{M_{\pi\pi}^2 - M_\rho^2 + iM_\rho\Gamma_\rho(M_{\pi\pi})} - B\right|^2. \tag{1.6}$$

We will stick to this expression in what follows.

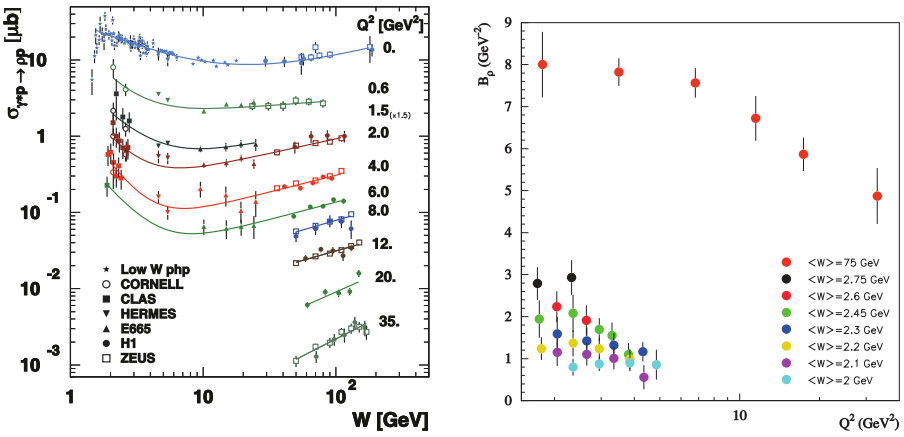

(a) Total cross section. (b) t slope.

Figure 1.6: W and Q^2 dependence of the $\gamma^* p \to \rho p$ cross section [10].

Observed dependences of the cross section

The diffractive $\gamma p \to \rho p$ cross section has been studied at various center-of-mass energies W and photon virtualities $Q^2 \equiv -q^2$. The low-W and low-Q^2 part of the phase-space was measured at fixed target experiments. The H1 and ZEUS collaborations at HERA were able to provide measurements [17, 18, 14, 15] for W up to 200 GeV and Q^2 up to 35 GeV^2. The elastic cross section as a function of W and Q^2 is shown on figure 1.6a.

The W dependence of the exclusive cross section can be parametrized as the sum of two power laws:

$$\sigma_{\gamma p \to \rho p} = \sigma_M W^{-\eta} + \sigma_{\mathbb{P}} W^{\epsilon}, \tag{1.7}$$

where, as in equation (1.3), σ_M stands for meson exchange and $\sigma_{\mathbb{P}}$ for pomeron exchange.

The t dependence of the cross section was measured at H1, ZEUS and other lower-energy experiments. Available data is well described by a decreasing exponential:

$$\frac{\mathrm{d}\sigma_{\gamma p \to V p}}{\mathrm{d}|t|} \propto e^{-b|t|}, \tag{1.8}$$

where the parameter b is called the t slope of the cross section, and is interpreted as the transverse area of the proton-photon system.

The observed b slope increases at high W (figure 1.6b); H1 and ZEUS found values around $b \approx 8\,\mathrm{GeV}^{-2}$ for $\langle W \rangle = 75\,\mathrm{GeV}$. In addition, the H1 collaboration found a slight deviation from a pure exponential above $|t| \sim 0.4\,\mathrm{GeV}^2$; ZEUS results weren't conclusive.

1.4 Ultra-peripheral collisions

When throwing a proton at a nucleus, it is likely that they will miss each other. In this case however, there is still a substantial probability for them to interact through their respective electromagnetic fields. Such a process is

called an ultra-peripheral collision (UPC for short), because it happens at a long distance from the nucleus.

Two classes of processes are possible in UPCs: photon-photon interactions, and strong interactions between a photon and one of the nuclei. In heavy ion-proton collisions, photon-proton interactions dominate because of the higher charge of the nucleus. This is one of the ways of probing vector meson photoproduction at high energy.

In order to extract photon-proton cross sections, it is crucial to know the energy spectrum of the involved photons. This computation is usually performed in the Weizsäcker-Williams approximation, whose derivation will be sketched. Since we are interested in the t-differential cross section, we will check that the transverse momentum of the photons is small. But before doing anything, let's define the kinematics.

Kinematics

We assign momenta k and k' to the incoming and outgoing lead nucleus:

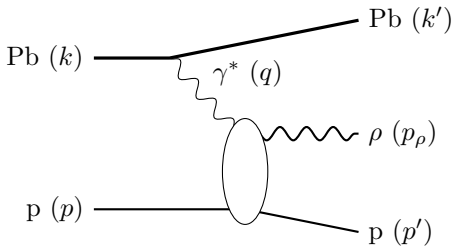

Other momenta are defined as before. We use a frame in which both the lead and the proton are ultrarelativistic, and neglect their masses with respect to their energy and axial momentum. Since this corresponds to the situation at a particle collider, we will call it the lab frame.

The Weizsäcker-Williams approximation

The Weizsäcker-Williams approximation can be used to compute the average number density of photons that accompany a charged particle moving close to the speed of light. Such a result is needed in order to describe ion-proton collisions in terms of photon-proton interactions. Before applying it to this particular case, let's first sketch its derivation.

The four-potential $\mathscr{A}^\mu$ of a moving charged particle can be computed in classical electrodynamics. It is traditionally written as a function of the position, $\mathscr{A}^\mu(x^\nu)$, or the momentum, $\mathscr{A}^\mu(q^\nu)$. The two representations are related by a Fourier transform. We'll use a mixed representation[3]: $\mathscr{A}^\mu(E_\gamma, \mathbf{b}, q^z)$, where E_γ is the energy, $\mathbf{b} \equiv (x, y)$ and q^z is the z component of the momentum.

We are, however, not interested in $\mathscr{A}^\mu$, but in the energy density[4] $\mathcal{E}$. If a spherical particle of charge Z is moving along the z axis in the $+z$ direction,

[3] At the cost of losing manifest Lorentz invariance.

and γ is the boost factor, one finds:

$$\mathcal{E}(E_\gamma, \mathbf{b}) = \frac{\alpha Z^2}{\pi^2} \frac{(E_\gamma)^2}{\gamma^2} K_1^2\left(\frac{bE_\gamma}{\gamma}\right),$$

where we have neglected terms of order $1/\gamma^2$ in the argument of K_1, $b = |\mathbf{b}|$, K_1 is the usual Bessel function and we have performed an integration over q^z.

The average energy- and impact parameter-dependent photon number density $\mathcal{N}$ is therefore given by:

$$\mathcal{N}(E_\gamma, \mathbf{b}) = \frac{1}{E_\gamma}\mathcal{E}(E_\gamma, \mathbf{b}) = \frac{\alpha Z^2}{\pi^2} \frac{E_\gamma}{\gamma^2} K_1^2\left(\frac{bE_\gamma}{\gamma}\right). \tag{1.9}$$

Let's now apply this result to ultra-peripheral collisions. There are several prescriptions on how to deal with the remaining dependence on the impact parameter $\mathbf{b}$. An analytical result can be obtained by integrating over the whole plane except the region $b < b_{\min}$, effectively describing the heavy ion as a hard sphere. Swapping E_γ for W, we find the following photon number density:

$$\Gamma(W) \equiv \frac{\mathrm{d}n_\gamma}{\mathrm{d}W} = \frac{\alpha Z^2}{\pi} \frac{2}{W}\Big[x^2\big(K_0^2(x) - K_1^2(x)\big) + 2xK_0(x)K_1(x)\Big], \tag{1.10}$$

where $x \equiv b_{\min}E_\gamma/\gamma = b_{\min}W^2/4\gamma E_p$.

Another method is to perform a Glauber calculation, taking into account the impact-parameter dependent probability of hitting the nucleus:

$$\Gamma(E_\gamma) = \int \mathrm{d}\mathbf{b}\,\mathcal{N}(E_\gamma, \mathbf{b})\big(1 - \mathrm{P(interaction)}(\mathbf{b})\big). \tag{1.11}$$

This second formula gives more precise results because it takes the nuclear density into account. In ion-ion collisions, the cross section is reduced by up to 20 % when compared to equation (1.10) [20].

Photon virtuality and transverse momentum

In order to measure the t slope of the photon-proton cross section, we must compute this variable from the kinematics of the ρ meson alone – we won't measure the scattered proton. In this section, we claim that equation (1.1) is still valid for ultra-peripheral collisions in the lab frame. This proposition can be formulated in three equivalent ways:

1. Equation (1.1) is valid in the lab frame;
2. The transverse boost needed to go from the lab frame to the photon-proton center-of-mass frame is small;

[4] In an arbitrary representation, the energy density can be computed as [19]:

$$\mathcal{E} = \frac{1}{2}(\hat{q}_{[i}\mathscr{A}_{0]})^2 + \frac{1}{4}(\hat{q}_{[i}\mathscr{A}_{j]})^2,$$

where $\hat{q}_i$ are the momentum operators. In position representation, one should take $\hat{q}_i = \partial_i$; in momentum representation, $\hat{q}_i = q_i$. In the expression above, $a_{[i}b_{j]}$ stands for $a_ib_j - a_jb_i$ and a sum over all free indices is implied after taking the square.

3. The transverse momentum of the photon is small.

The last formulation makes it clear that one should take the ion into account, because that's where the photon gets produced.

The structure of the ion can be described using its form factor $F(q^\mu)$, defined as the Fourier transform of its charge distribution. Assuming a Woods-Saxon matter distribution, one can show that an approximate form factor is given by [20]:

$$F(q^\mu) = \Big[\sin(QR) - QR\cos(QR)\Big]\frac{3}{(QR)^3}\frac{1}{1+a^2Q^2}, \tag{1.12}$$

where R is the nuclear radius, a is fixed to $0.57\,\mathrm{GeV}^{-1}$ and $Q^2 \equiv -q^2 \geq 0$ is the virtuality of the photon. In the lab frame, it can be written as:

$$Q^2 = \frac{E_\gamma^2}{\gamma^2} + (p_t^\gamma)^2,$$

where γ is the Lorentz boost of the ion and p_t^γ the photon transverse momentum. Using this expression, one can compute the average photon virtuality at a given photon energy:

$$\langle Q^2 \rangle = \frac{\int_{E_\gamma^2/\gamma^2}^{\infty} \mathrm{d}Q^2\, Q^2 F^2(Q^2)}{\int_{E_\gamma^2/\gamma^2}^{\infty} \mathrm{d}Q^2\, F^2(Q^2)}.$$

Evaluating this expression for lead ($R = 5.343\,\mathrm{GeV}^{-1}$) and typical photon energies at the LHC gives $\langle Q^2 \rangle \approx 0.025\,\mathrm{GeV}^2$. This value is also an upper bound for the square of the photon transverse momentum $(p_t^\gamma)^2 < Q^2$. Expression (1.1) is therefore valid in the lab frame from approximately $\Delta t \sim 0.025\,\mathrm{GeV}^2$ upwards, and we can use it.

1.5 Monte-Carlo simulations

Modern particle physics experiments are increasingly complex. The size of the detectors, the amount of data they collect and the number of processing steps needed in order to get usable high-level objects (reconstructed particles etc) makes it impossible for an human to understand all experimental effects, let alone find an analytic description.

In order to relieve themselves from this challenge, particle physicists use detailed computer simulations of their detectors. Such simulations are used to check that the observed distributions match the predictions, but also to correct for acceptance and detection efficiency. These simulations play a central role in virtually every modern particle physics data analysis.

Simulated events are not chosen at random, but usually follow expected physical distribution. This has several advantages: the same simulations can be used to predict expected number of events and to perform the analysis; deviations from predictions can be spotted earlier; the uncertainty on total cross sections is minimized. The main drawback of this approach is that it causes large uncertainties in regions of the phase space where the cross section is small, because of the lower statistics available to estimate the detector response.

There is a large family of Monte-Carlo event generators, programs that produce events according to known (or predicted) cross sections. Such programs exist for a wide range of processes, from production of hypothetical particles to the well-known quantum electrodynamics. Event generators are experiment-agnostic (except for the initial state), and the same generator is often used by several experiments.

The STARlight event generator

STARlight [20] is an event generator that produces UPC events using the current knowledge of the cross sections. It targets high-energy experiments such as the RHIC and the LHC. STARlight supports two production modes, two-photon and photonuclear interactions, and a wide range of final states. It can also simulate nuclear breakup.

Among the channels supported by STARlight are diffractive production of the ρ^0, ω, ϕ and ρ' vector mesons, including interference of the ρ^0 with direct $\pi^+\pi^-$ production. It can't, however, simulate three-body decays such as $\omega \to \pi^+\pi^-\pi^0$. Due to the lack of available data, some of its parameters are guesses that should not be relied upon; this is in particular the case for the ρ' resonance.

STARlight uses equation (1.11) to compute the photon flux. It assumes vector meson dominance and describes the vector meson total cross sections using equation (1.3). The transverse momentum dependence of the cross section is evaluated by performing the following integral:

$$\left.\frac{\mathrm{d}\sigma_{Ap\to AVp}}{\mathrm{d}\mathbf{p}_t^V}\right|_{\mathbf{p}_t^V, M_V^2, E_\gamma} \propto \int \mathrm{d}^2\mathbf{p}_t^\gamma \left(\Gamma_A(E_\gamma)\,\frac{(\mathbf{p}_t^\gamma)^2}{q^4} F_A^2(q)\,F_p^2(\Delta) + (p \leftrightarrow A)\right),$$

where Δ is the four-momentum transfer at the proton vertex, q and $\mathbf{p}_t^\gamma$ are respectively the four- and transverse momentums of the photon, and E_γ is its energy. Γ_A is the photon flux for nucleus A. F_A is the nucleus form factor of equation (1.12) and F_p is the proton form factor:

$$F_p(\Delta) = \left[1 + \frac{\Delta^2}{\Delta_0^2}\right]^{-2},$$

corresponding to an exponential charge distribution. The proton "radius" Δ_0^2 is fixed to $0.71\,\mathrm{GeV}^2$.

Chapter 2

Experimental setup

In this chapter, we describe the experimental setup that was produced the data used in our analysis. We will begin with the accelerator used to produce the beams. The main section covers the detector itself, or rather the different subdetectors it is made of. In the last section, we will briefly describe how the data is preprocessed to make it usable for physics analyses.

2.1 The LHC

The Large Hadron Collider (LHC) is a circular particle collider located at CERN, Geneva. Its two beams meet each other at four points, shared by seven detectors. There are four big detectors (ALICE, ATLAS, CMS and LHCb) and three smaller ones (LHCf, MoEDAL and TOTEM). Two of them (ATLAS and CMS) are generalist and aim at very diverse physics programmes; the others were designed to study more specific topics.

The LHC beams are not continuous: particles are bunched together, with a nominal bunch crossing rate of 40 MHz. The LHC is the highest-energy part of a chain of particle accelerators operated by CERN. Before being sent to the LHC, bunches are formed and pre-accelerated by several other facilities, some of them taking their roots back in the fifties. The full accelerator complex is represented on figure 2.1.

Despite its ability to accelerate heavy ions, the LHC operates most of the time in proton-proton mode. Between the start of the data-taking in 2010 and the first long shutdown in 2013, only one month of Pb-Pb data was taken, and another month was split into p-Pb and Pb-p data.

2.2 The CMS detector

CMS (Compact Muon Solenoid) [22] is one of the four main detectors using the LHC colliding beams. It is built around a large superconducting solenoid that produces the strong 4 T magnetic field necessary to bend the trajectory of high momentum charged particles. A silicon tracking system and two calorimeters are located inside the magnet. Around it is built a big tracking system dedicated to muons – hence the name of the experiment.

CMS can detect almost every long-lived particle of the Standard Model, with only neutrinos escaping without being seen. It achieves this through the

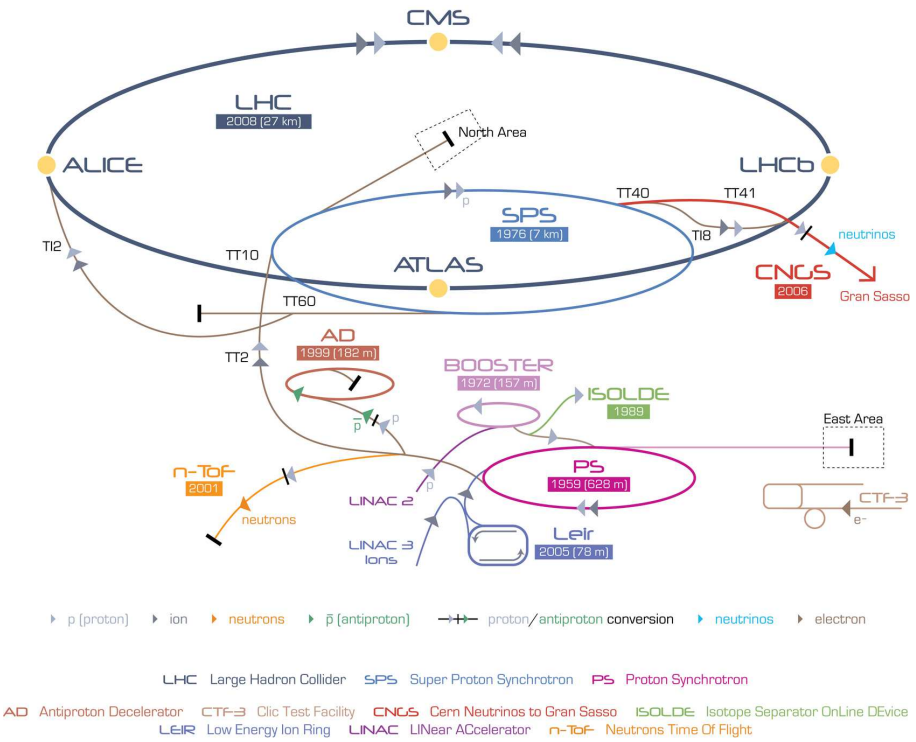

Figure 2.1: The CERN accelerator complex in 2012, and the main experiments at the time [21].

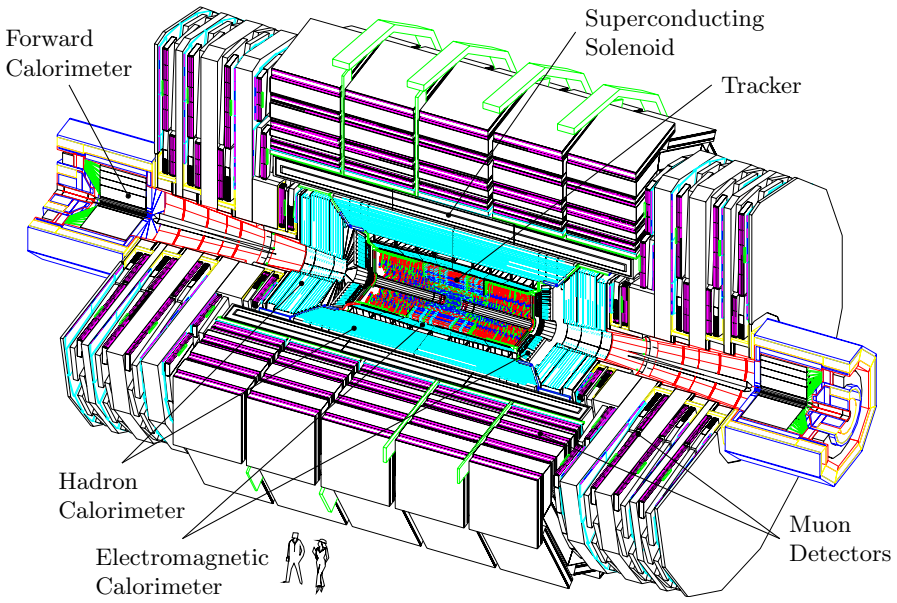

Figure 2.2: A perspective view of the CMS detector (adapted from [22]). ZDC and CASTOR are not represented.

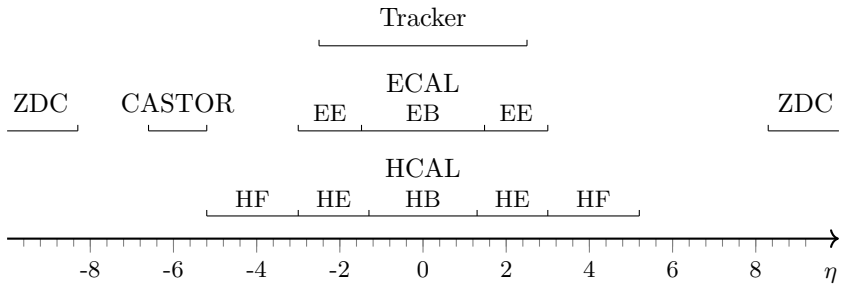

Figure 2.3: Pseudorapidity coverage of the various CMS subdetectors.

combination of different detection techniques (see figure 2.2). The apparatus closest to the interaction point is a large silicon tracker, sensitive to charged particles going through it. It is surrounded by an electromagnetic calorimeter that measures the energy of high-energy photons and electrons, and a hadronic calorimeter that does the same for hadrons. The muon tracking system that surrounds the magnet won't be of interest to us in the present analysis.

Most of the CMS instruments are concentrated in the mid-rapidity region. The tracker covers the range $|\eta| < 2.5$; the electromagnetic calorimeter (ECAL) extends to $|\eta| < 3.0$, and the hadronic calorimeter (HCAL) to $|\eta| < 5.2$. Additional calorimeters, CASTOR and ZDC, cover the ranges $-6.6 < \eta < -5.2$ and $|\eta| > 8.3$ respectively. Figure 2.3 shows the extent of the various subdetectors.

We now proceed to a more in-depth description of the detectors that will be used in this analysis: the tracker, the electromagnetic and hadronic calorimeters, CASTOR and ZDC.

The tracker

The innermost part of CMS, the tracker, was designed to be able to reconstruct the individual trajectories of more than 1 000 particles in a single bunch crossing. Radiation damage and the need to limit the material budget were other design challenges. With about $200\,\mathrm{m}^2$ of active area, CMS uses the larges silicon tracker ever built.

The innermost part of the tracker is a pixel detector composed of three concentric barrels of radii from 4.4 to 10.2 cm, supplemented by two endcaps. It covers pseudorapidities in the range $|\eta| < 2.5$. With a pixel size of $100 \times 150\,\mu\mathrm{m}^2$, it provides the high spatial resolution needed to distinguish between many primary and secondary vertices.

Around the pixel detector, the tracker is made of several barrels and endcaps of strip sensors, up to a radius of 1.14 m. Its geometry is such that all tracks within $|\eta| < 2.4$ cross at least 9 layers, with 4 of them providing directional information. Like the pixel detector, the strip sensors' acceptance extends to $|\eta| < 2.5$.

The tracking system as a whole is able to reconstruct charged particles' trajectories in three dimensions. Thanks to the strong magnetic field, there is a relation between the track curvature and the transverse momentum p_t of the corresponding particle:

$$p_t[\mathrm{GeV}] = 0.3\, B[\mathrm{T}] R[\mathrm{m}],$$

where B is the magnetic field and $R > 0$ is the radius of the track. The sign of the curvature gives the sign of the charge of the particle; we will call it the track "sign" below.

The track parameters are inferred form the measured points using a Kalman filter, an iterative generalization of least-squares fitting to systems undergoing random evolution (but with with modeled randomness) [23]. The Kalman filter is able to estimate the measurement error; for low-energy particles, multiple scattering dominates. A quick analysis of our data (see chapter 3) gave us a resolution of $\Delta p_t/p_t \lesssim 3\,\%$.

The electromagnetic calorimeter

The electromagnetic calorimeter (ECAL for short) is made of 75 848 $PbWO_4$ crystals, each of them about 25 radiation lengths-deep. It provides an hermetic coverage of the pseudorapidity range $|\eta| < 3.0$. It measures the energy of photons and ultrarelativistic electrons through the cascade they produce in the absorber material.

The barrel part (EB) is 360-fold in ϕ and 2×85-fold in η, so that each crystal covers approximately $\Delta\eta \times \Delta\phi \approx 0.0174 \times 0.0174$. It covers the pseudorapidity range $|\eta| < 1.479$; its inner radius is about 1.29 m. In order to avoid the effect of radial cracks in the structure, the crystals do not point straight to the interaction point, but are instead tilted by 3°.

Each of two endcaps (EE) is made of 7 324 crystals arranged in a grid in the x-y plane. They are located at 3.154 m from the interaction point, and cover the pseudorapidity range $1.5 < |\eta| < 3.0$. Like in the barrel part, the crystals are tilted (by 2° to 8°) to avoid cracks effects.

The energy resolution of a calorimeter can be parametrized as:

$$\left(\frac{\sigma_E}{E}\right)^2 = \left(\frac{S}{\sqrt{E}}\right)^2 + \left(\frac{N}{E}\right)^2 + C^2,$$

where S is the stochastic term, N is the noise term and C is the constant term. For the ECAL, S was found to be about $5\,\% \times \sqrt{\text{GeV}}$; a value of C below 0.3 % was part of the design requirements. The noise term is dominated by electronics and digitization; one has $N \approx 40\,\text{MeV}$, and the noise has a clean gaussian shape.

The hadron calorimeter

Located just behind its electromagnetic counterpart, the hadronic calorimeter (HCAL) has a lower spatial resolution but covers a larger rapidity range, down to $|\eta| < 5.2$. It is made of six sections: a barrel (HB), two endcaps (HE) and two "forward" parts (HF). The sixth part, the "outer" calorimeter, surrounds the solenoid to catch the tails of high-energy cascades, and is of little interest to us.

Hadrons sometimes start cascading in the ECAL, before reaching HB or HE. In this case, the ECAL provides additional measurements that are combined with those of the HCAL.

The barrel part covers the range $|\eta| < 1.3$. It is 2×16-fold in η and 72-fold in ϕ, for a spatial resolution $\Delta\eta \times \Delta\phi \approx 0.087 \times 0.087$. Every HB cell maps to

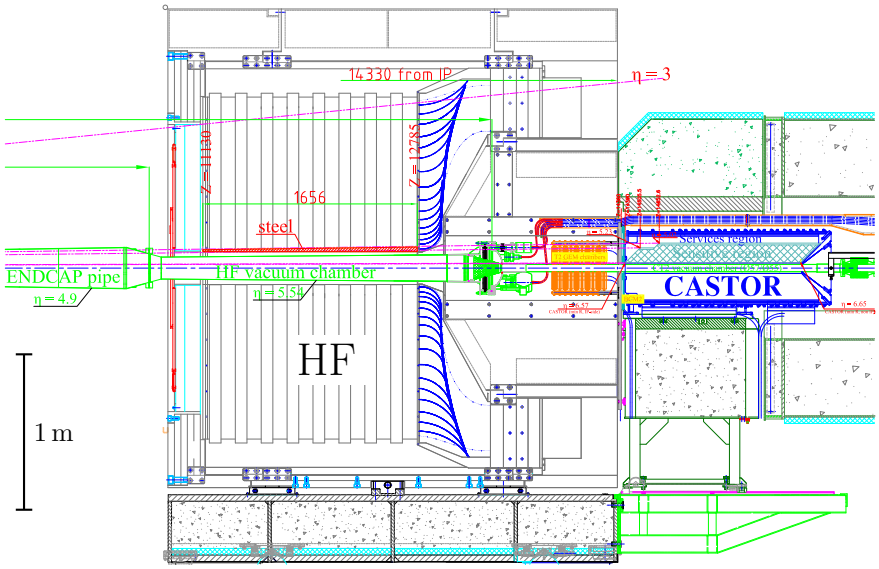

Figure 2.4: Location of HF and CASTOR (adapted from [24]). Despite the positive values of η on the diagram, CASTOR is located in the negative η region. The orange device in front of CASTOR is part of the TOTEM detector.

a group of 5 by 5 crystals in EB. HB is made of 14 brass plates stacked above each other, with plastic scintillator layers interleaved in-between. The total depth goes from 5.82 interaction lengths (λ_I) at $\eta = 0$ to $10.6\lambda_I$ at $|\eta| = 1.3$.

The two endcaps cover the range $1.3 < |\eta| < 3.0$. For $|\eta| < 1.6$, their granularity is the same as in the barrel, $\Delta\eta \times \Delta\phi \approx 0.087 \times 0.087$. It is lower for $|\eta| \geq 1.6$, $\Delta\eta \times \Delta\phi \approx 0.17 \times 0.17$. The same brass alloy as in HB is used; taking the ECAL into account, the two HE are about 10 interaction lengths-deep.

HF extends the HCAL to the pseudorapidity range $|\eta| < 5.2$. Its granularity is mostly $\Delta\eta \times \Delta\phi = 0.175 \times 0.175$. HF can distinguish showers generated by electrons and photons, whose starting depth is lower than for hadronic ones. It uses steel as its absorber material, and uses the Cherenkov light emitted by charged particles to detect them.

CASTOR

CASTOR (Centauro and STrange Object Research) is a Cherenkov detector located on the $-z$ side of CMS, covering the pseudorapidity range $-6.6 < \eta < -5.2$. It is located as close to the beam pipe as one can get (1 cm); see figure 2.4 for its location relative to HF. CASTOR can be taken away from the beam if needed.

The design of CASTOR allows it to be sensitive to anything ranging from a single minimum ionizing particle to jets at full beam energy (7 TeV). It has two electromagnetic sections and twelve hadronic ones. A 16-fold division in ϕ

allows for a resolution of about 20 degrees. All in all, the CASTOR signal is split into 224 channels.

The zero-degree calorimeters

The zero-degree calorimeters (ZDC) surround the beam pipes on each side of the z axis, at a distance of 140 m from the interaction point. This location allows them to cover the pseudorapidity range $|\eta| > 8.3$ for neutral particles (mostly photons and neutrons). They have a 19 radiation lengths-deep electromagnetic section, and a $6.5\lambda_I$ hadronic section. They are able to reconstruct the energy of 2.75 TeV neutrons with a resolution above 15 %. As CASTOR, the ZDC are removed from the detector during high-luminosity runs.

2.3 Data processing system

Not all events happening at the LHC are equally interesting. Moreover, the amount of data produced by a big detector like CMS running at 40 MHz is huge. Recording every single event is thus impossible, and a way to decide which events to keep is needed. This is achieved by a complex system of triggers. In this section, we summarize the design of the event selection and reconstruction system.

The selection of events to be recorded is done in two steps. A first selection is performed in hardware (mostly programmable electronics), bringing the event rate down to 100 kHz; this is called the Level-1 (L1) trigger. Events accepted by the L1 trigger are forwarded to a computer farm, which further reduces the output rate, down to 100 Hz. More subdetector data (in particular the tracker) is available for this step, called the high-level trigger (HLT).

Events selected by the HLT are saved and dispatched to data centers around the World, where they undergo several processing steps in order to reconstruct physical information. The data produced at CMS and the other major LHC experiments is processed by the largest single-purpose distributed computing grid ever built.

Chapter 3

Event samples

In this analysis, we use proton-lead and lead-proton data taken by CMS for three weeks during the winter 2013. At that time, the LHC was being operated at an energy of 4 TeV per proton and 1.58 TeV per lead nucleon, which corresponds to a nucleon-to-nucleon center-of-mass energy $\sqrt{s_{NN}} = 5.02\,\text{TeV}$.

The expected signature of our events consists in two tracks of opposite charges and nothing else in the detector.

Since the tracker does not provide L1 triggers, we use the so-called "zero bias" trigger, which records a given (small) fraction of all active bunch crossings. The zero bias data mostly contains empty events, with only a fraction of the data being useful. Out of the 287 million events recorded by the zero bias trigger, only about 160 000 contain two or more reconstructed tracks.

The integrated luminosity for the 2013 zero-bias dataset is $16.94\,\mu\text{b}^{-1}$, of which $7.39\,\mu\text{b}^{-1}$ is proton-lead data and $9.55\,\mu\text{b}^{-1}$ is lead-proton. These values are known to 3.6 % [25].

In this chapter, we describe how the detector was used to select an event sample corresponding to ρ^0 production, with a background contamination as low as possible. We will go roughly from the innermost detection layers to the outermost. We'll start with the selection of tracks, before investigating the cuts on energy deposit in the barrels of the ECAL and HCAL. The endcaps will then be given some attention before moving to the forward detectors, CASTOR and ZDC.

3.1 Tracks

Since the ρ^0 decays into two charged pions, the experimental signature in CMS for its exclusive production is two tracks of opposite signs. There must be nothing else in the detector. For this reason, the very first cut we apply is on the number of tracks: we require that there are exactly two.

In order to avoid tracks too close to the edges of the tracker, only those with $|\eta| < 2.4$ are kept; events with tracks outside of this range are thrown away. Likewise, in order to remove badly reconstructed tracks, the estimated χ^2/number of degrees of freedom (ndf) of both fits is required to be below 10. We also require all tracks to point to a single vertex.

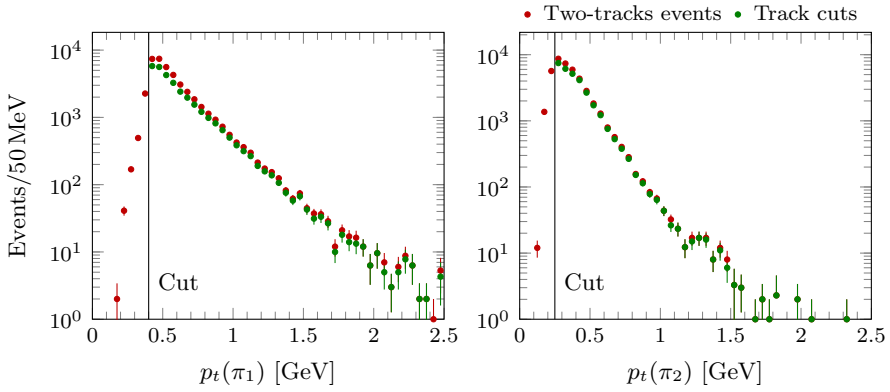

Figure 3.1: Track p_t before and after track cuts. The left plot shows the leading-p_t track, the right one the second track. The cut is also represented.

3.2 Background suppression

In order to avoid a not well controlled low-efficiency region, the leading-p_t track is required to have $p_t > 400\,\text{MeV}$, and the other one $p_t > 250\,\text{MeV}$. This cut reduces the acceptance at low $|t|$ and low ρ invariant mass.

In order to avoid contamination from the exclusive ϕ production with $\phi \to K^+K^-$, the invariant mass of the two tracks assuming $K^\pm$ mass, M_{KK}, is required to be above 1.04 GeV (the mass of the ϕ is 1.02 GeV and its width 4 MeV). It was shown at HERA that this cut removes most of the ϕ contribution [17].

The effect of these cuts is shown on figure 3.1, while the kinematics of the ρ candidate is shown on figure 3.2.

3.3 ECAL Barrel

A few particles can be detected only in EB. The ECAL is designed to reconstruct precisely the deposited energy of photons and electrons/positrons. But at low energy, hadrons will be stopped by the ECAL. It has been checked that the charged pions from the ρ decay do not leave signal in the ECAL above the noise level (by trying to correlate hits and tracks). This was to be expected, since low-p_t charged particles cannot exit the tracker because of the magnetic field and stochastic energy loss.

Neutral pions, that decay into two photons, are possibly visible. Backgrounds such as the $\omega \to \pi^+\pi^-\pi^0$ may be reduced using the ECAL, especially at high transverse momentum. Overall, one doesn't expect events with lots of hits in the ECAL.

The objects used in this analysis to evaluate activity in EB are the so-called `CaloTowers`. `CaloTowers` offer an unified formalism to deal with information from all CMS calorimeters. They are used by CMSSW to reconstruct photons, electrons, missing transverse momentum and jets. `CaloTowers`' information is calibrated.

In EB, `CaloTowers` aggregate information from groups of 5 by 5 crystals. One can extract the mean η and ϕ, as well as the total energy E_{em} and the

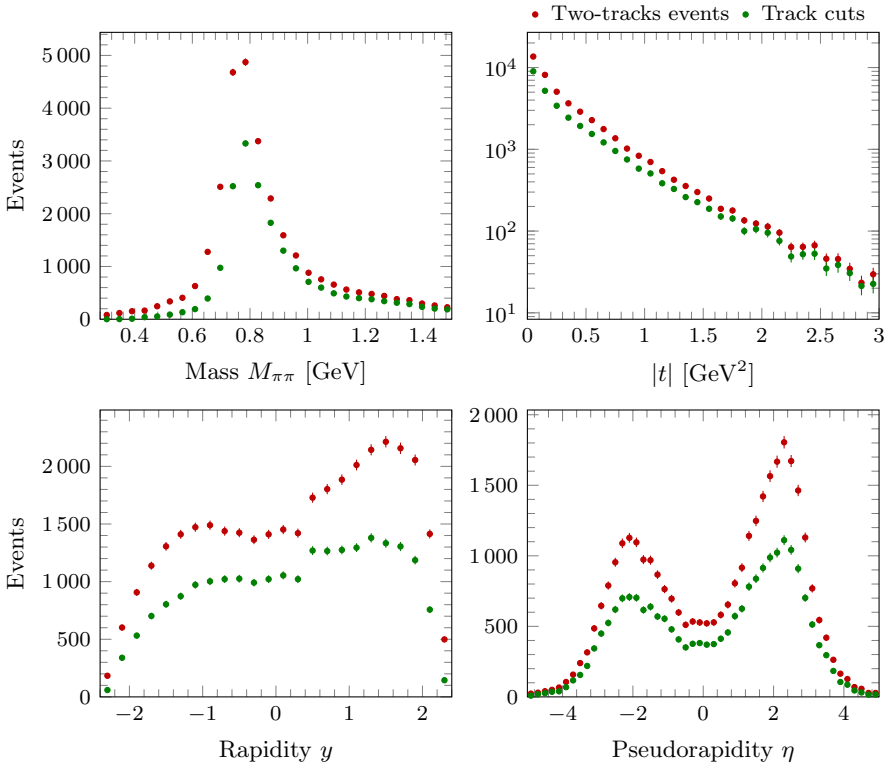

Figure 3.2: Kinematics of the ρ candidate before and after track cuts. Visible differences include a slight decrease of the $|t|$ slope and the removal of most events at low invariant mass. Both effects are consequences of the cut on track p_t. $y > 0$ corresponds to the direction of the photon (or lead).

number N_{em} of crystals that have been hit. Since towers with a total energy below 200 MeV are filtered out to save disk space, we can't use them – but we'll see that they wouldn't be useful anyway.

Hot Cells

A quick look at the spatial distribution of hits in the ECAL (figure 3.3a) shows that most of them come from a small fraction of the towers, that we will call "hot" in what follows – there are a dozen of them, out of one thousand towers. Moreover, one can distinguish rectangles in the (η, ϕ) plane where there are more hits than in the average. Such variations can't come from particles reaching EB, which would be produced uniformly in ϕ.

Looking closer, one identify that just a few crystals cause the whole hot cells signal. However, there is no (easy) way to tell apart individual crystals from `CaloTowers` on an event-by-event basis. In order to avoid the hot part of the signal, we must therefore ignore anything coming from hot towers – not just when a hot crystal fires up.

The precise set of towers to be neglected was defined by hand, with no systematic criteria – but with the implicit goal of reaching a better spatial

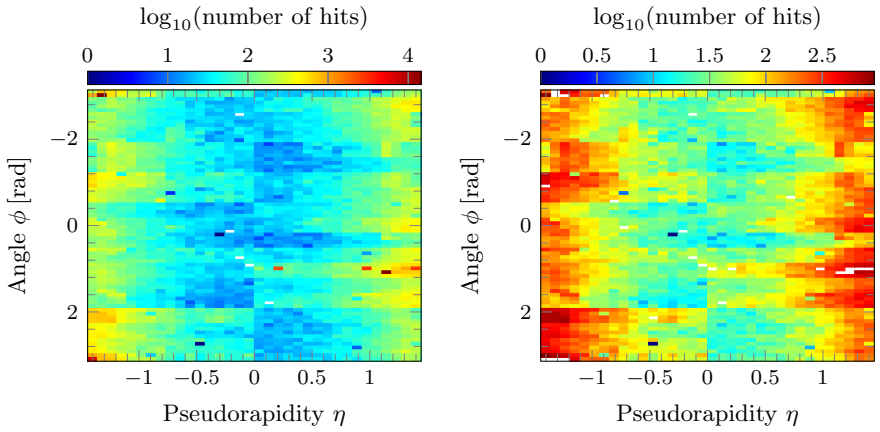

(a) Before hot cells removal.

(b) After hot cells removal.

Figure 3.3: Spatial distribution of towers in EB with $E_{\text{em}} > 0.5\,\text{GeV}$, before and after hot towers removal. Notice the logarithmic scales.

distribution. A total of 22 towers (out of 1224) are ignored; the fraction of the phase space that is lost (about 2 %) can be neglected, as will be shown later.

Cut

`CaloTowers` aggregate several crystals, but the noise is expected to come from individual crystals (in particular from their readout electronics). In order to separate signal from noise, a cut using `CaloTowers` is expected to use the number of crystals N_{em} considered for building towers' energy.

An histogram of N_{em} for all (not hot) towers is shown on figure 3.4a. That the most probable number of crystals be greater than one is clearly unphysical, as low-energy particles' showers aren't expected to span multiple crystals, and high-energy particles are rare.

Looking at the mean energy per crystal, $\langle E_{\text{em}} \rangle \equiv E_{\text{em}}/N_{\text{em}}$ (figure 3.4b), we can assume that the low-energy bump corresponds to noise, while the higher-energy tail is signal. This hypothesis is supported by our knowledge of the electronic noise, which has a 40 MeV-wide gaussian shape.

In order to test our assumption, we define cuts and make some tests. We'll among others check that the spatial distribution of the tail is uniform and that the number of hits is zero for most of the ρ events. The cuts we use are:

$$\text{good tower} \equiv \frac{E_{\text{em}}}{N_{\text{em}}} > \begin{cases} 0.36\,\text{GeV} & \text{if } N_{\text{em}} = 1, \\ 0.29\,\text{GeV} & \text{if } N_{\text{em}} = 2, \\ 0.26\,\text{GeV} & \text{if } N_{\text{em}} = 3, \\ 0.24\,\text{GeV} & \text{if } N_{\text{em}} = 4, \\ 0.22\,\text{GeV} & \text{else.} \end{cases}$$

They are represented on figure 3.4b.

The very first check we do is to plot the number of crystals per good tower, as is done in figure 3.4a. One can see that the most probable number of hits is

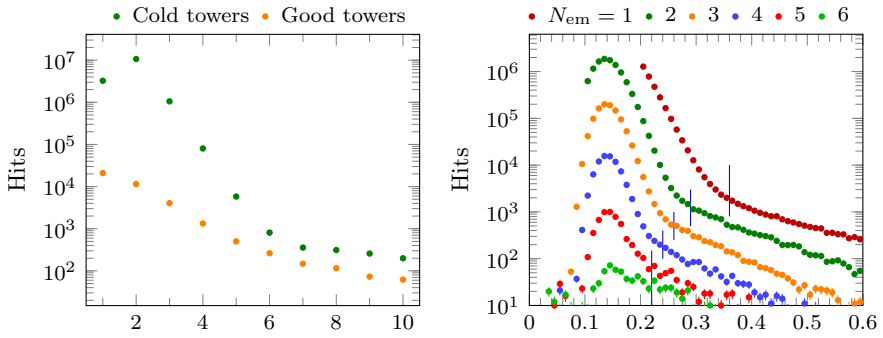

(a) Number of crystals N_{em}.

(b) Mean energy $\langle E_{\text{em}} \rangle$ [GeV].

Figure 3.4: Properties of `CaloTowers` in EB. Energy cuts are represented on the second graph. "Cold" towers are those that are not hot; "good" towers are those that pass the cuts. Events with $N_{\text{em}} = 0$ are not shown.

now 1, as expected. As a second test, the spatial distribution (figure 3.5a) is now uniform in ϕ. Moreover, the hit multiplicity (figure 3.5b) is zero for most events, and is lower in the average when other exclusivity cuts are applied. The EB cut is thus correlated to other cuts, which is encouraging.

The last check before looking at the effect on the properties of the ρ meson is to look at the photon-photon invariant mass distribution for two-hits events (figure 3.5c). One can clearly see a sharp peak around 100 MeV. This is roughly the mass of the π^0, which decays into two photons.

Since all checks tend to agree, we can now be confident that the signal is indeed caused by particles reaching the ECAL. Let's take a look at what happens to the ρ kinematics when using EB as an exclusivity cut, i.e. when rejecting events with at least one good `CaloTower`.

Effect of the Cut

In order to evaluate the effect of the EB cut, we plot on figure 3.6 the ρ kinematics with all cuts defined in this chapter applied (including those that were not yet mentioned), and the same without the EB cut. This presentation emphasizes events that are rejected by the EB cut only.

Let's see what the effect of using EB as an exclusivity criterion is. If the EB cut allows to reject events with photons from π^0's or other decays from background events, we expect a change in the $|t|$ slope, and maybe a slight sharpening of the mass peak. On figure 3.6, we plot these two distributions with all cuts defined in the present chapter applied, and with all cuts but the EB one. The two aforementioned effects are indeed visible.

On its own, the EB cut excludes a thousand out of around 20 000 events. Since hot towers add up to only 2 % of the phase space, we can neglect the effect of having ignored them – taking it into account would remove an additional 20 events.

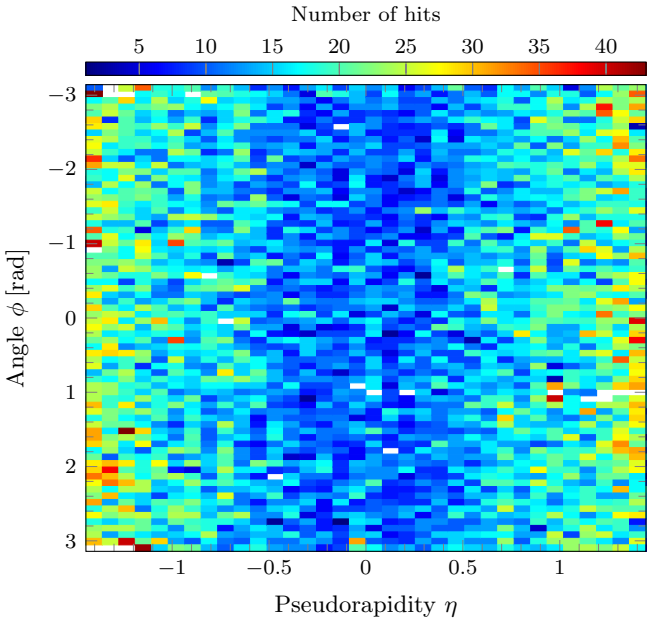

(a) Spatial distribution. Notice that the scale is now linear.

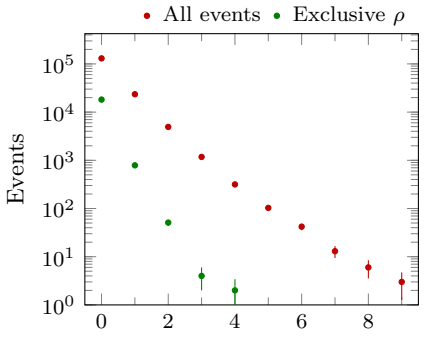

(b) Multiplicity.

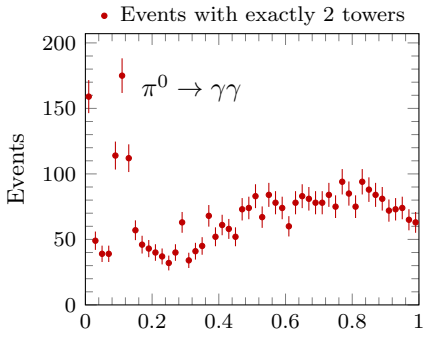

(c) Pair mass $M_{\gamma\gamma}$ [GeV]

Figure 3.5: Properties of good EB towers. "All events" means events with 2 or more tracks; "exclusive ρ" means events with all exclusivity cuts applied, except of course the EB one. There aren't enough exclusive ρ events with two towers to make a useful $M_{\gamma\gamma}$ plot for these.

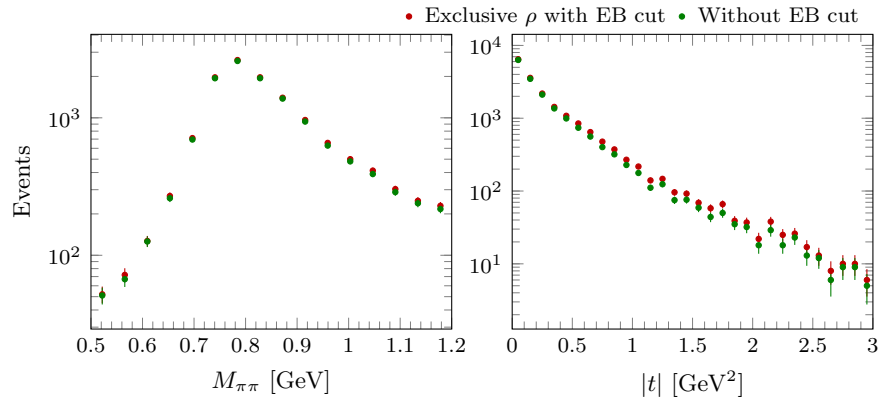

Figure 3.6: Effect of the EB cut. All exclusivity cuts defined in the present chapter are applied, except for the EB one. A larger fraction of events is removed out of the mass peak (left plot) and at high $|t|$ (right plot).

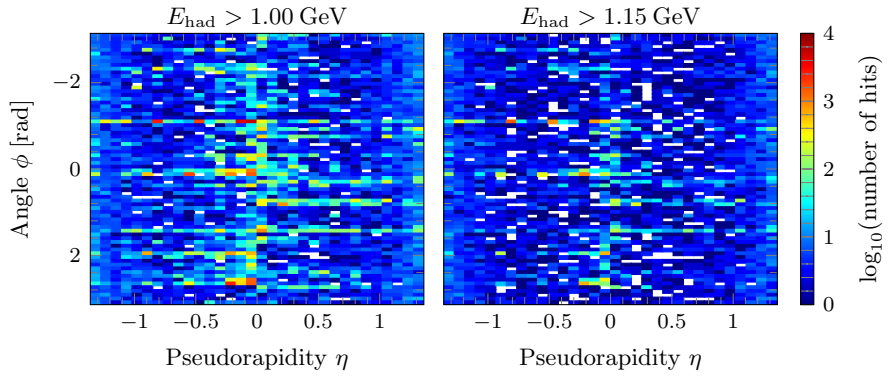

Figure 3.7: Spatial distribution of towers in HB above two threshold energies. Notice the logarithmic scale.

3.4 HCAL Barrel

Particles that can reach HB without being seen in the tracker or the ECAL are rare. They include only long-lived, neutral hadrons: neutrons and K_L^0's. Furthermore, hadronic showers often begin in the ECAL, and should be partially measurable there. As it is used in FSQ-16-007, we can nevertheless check if the HB can be used as an exclusivity criterion.

Like in EB, we use information from `CaloTowers` to evaluate activity in HB. Every HB tower maps to a single cell; there is no cell multiplicity. The spatial granularity of towers is the same as in EB.

Hot Cells

One of HB's peculiarities is the high number of hot cells, and its strong dependence on η and the threshold energy. Figure 3.7 shows the spatial distribution of hits with an energy above two different thresholds. Physical signal is ex-

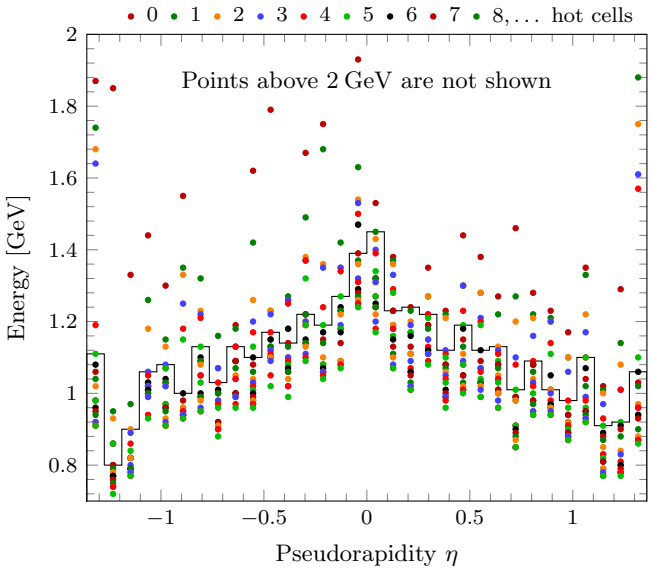

Figure 3.8: HB E^* as a function of the number of ignored cells. E^* is defined as the lowest energy cut for which the P-value for the ϕ distribution being uniform is higher than 1 %. The chosen cut is superimposed (black solid line).

pected to be uniform in ϕ; this is the case above 1 GeV in the high $|\eta|$ region, while it is not in the center, even above 1.15 GeV. A stringent cut should therefore both depend on η and ignore hot cells.

Since the number of possible cuts with a pseudorapidity-dependent threshold is very high, a semi-automated procedure was used. The HCAL is first split into rings, each of them being one cell wide in η and covering the full detector in ϕ:

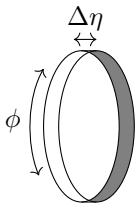

The uniformity of the distribution of hits in each wheel is measured using the P-value. The lowest energy cut for which the distribution remains uniform (with a P-value greater than 1%), E^*, is computed.

In order to take hot cells into account, this procedure can ignore a fixed number n of the most active cells. It was performed with values of n going from 0 to 20. The energy thresholds $E^*_n(\eta)$ are shown on figure 3.8 for values of n starting from 0. This plot should be read from top to bottom: The highest point in a given η bin is the highest energy for which the distribution in ϕ is uniform without ignoring any cell. The second point gives the same when ignoring one cell, and so on.

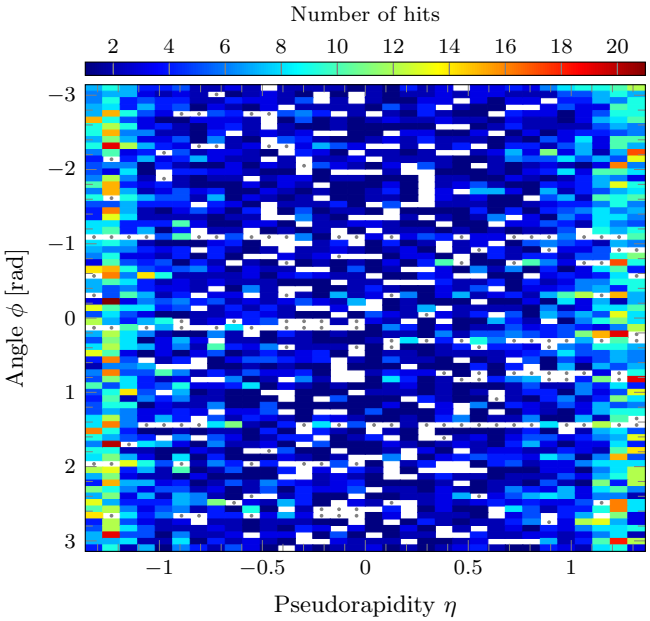

Figure 3.9: Spatial distribution of hits in the HCAL barrel, after hot cell removal. The ~ 120 ignored cells are marked with a gray dot.

Cut

One has to do a compromise between the number of cells that are ignored and the potential advantage of having a lower threshold. One can see on figure 3.8 that, while ignoring a few cells can lead to big energy gains (almost 1 GeV in the best case), there is at some point a saturation. Removing additional cells then leads to a very small benefit.

We choose to cut just below the lowest significant gap, which was chosen by hand (see the black line on figure 3.8); a total of about 120 cells are ignored this way (out of 1152). They are shown as gray dots on figure 3.9, together with the spatial distribution of hits passing the cut ("cold" ones).

Energy distributions of hits before and after applying the cut are plotted on figure 3.10. One can see that requiring spatial uniformity lead to a much smoother energy distribution, with a slope equal to the asymptotic one – the decrease below 1.2 GeV is due to the lower acceptance at low energy.

Effect of the cut

Let's now try to evaluate how useful HB can be for our analysis. For this, we select events without any good hit in HB; the effect of this cut on the ρ kinematics is shown on figure 3.11. We find that the number of events excluded by HB alone is negligible, and will therefore not use HB as an exclusivity criterion.

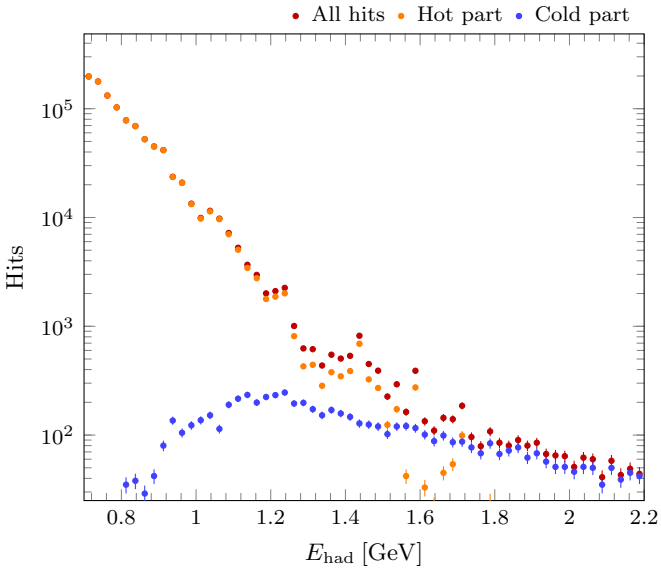

Figure 3.10: Energy distribution of hits in HB. The "hot" part corresponds to ignored cells; the "cold" part is what remains.

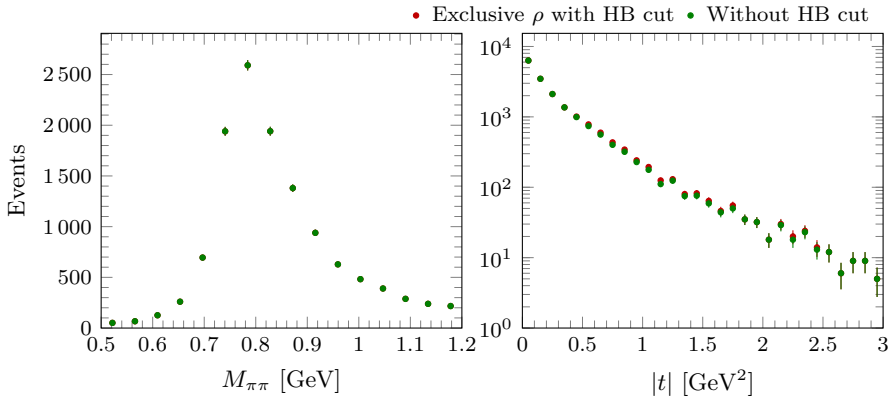

Figure 3.11: Effect of the HB cut. All exclusivity cuts defined in the present chapter are applied, except for the HB one. The fraction of otherwise exclusive events removed by HB is negligible.

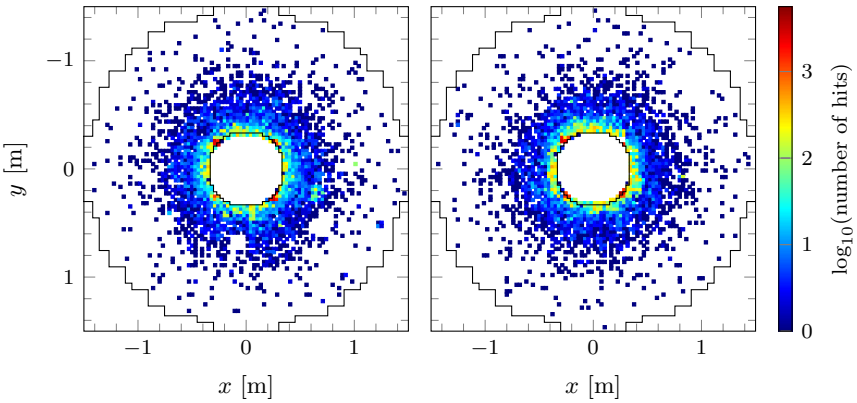

Figure 3.12: Hits in the ECAL endcaps with $E_{\text{em}} > 2\,\text{GeV}$ (left: EE−, right: EE+). The mapping to the (x, y) plane is approximate.

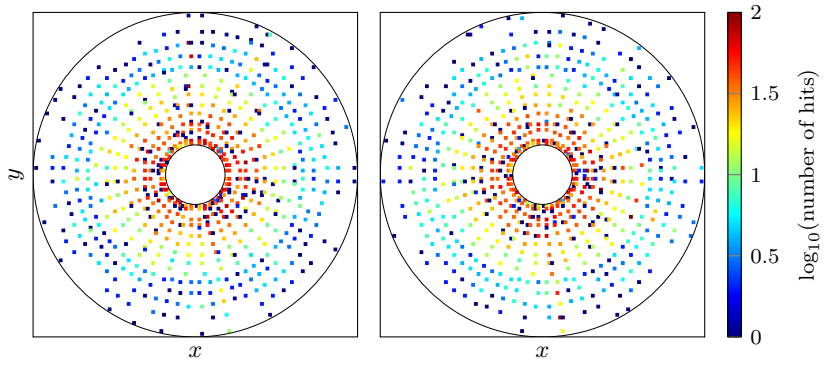

Figure 3.13: Hits in the HCAL endcaps with $E_{\text{had}} > 1.95\,\text{GeV}$ (left: HE−, right: HE+). The mapping of the detector geometry to the (x, y) plane is approximate.

3.5 Endcaps

We didn't have the time to study the endcaps as systematically as the barrels. We summarize our findings below, looking first at the ECAL endcaps, then at HB. HF will also be mentioned briefly.

The authors of FSQ-16-007 claim that the ECAL endcaps aren't useful to isolate an exclusive ρ sample. Since we saw that EB was dominated by hot cells, we looked at the spatial distribution of hits in EE (figure 3.12), with an energy threshold close to what the FSQ-16-007 authors used. While there appears to be hot cells near the inner edge of the endcap, ignoring them and using uniform cuts didn't lead to any significant change of the t and $M_{\pi\pi}$ distributions. As we didn't have the time to conduct the study for a pseudorapidity-dependent cut, we don't use EE in this analysis.

Unlike EE, the HCAL endcaps are used in FSQ-16-007, with an uniform energy threshold of 1.95 GeV. Figure 3.13 shows the spatial distribution of hits with an hadronic energy deposit above this cut. It is uniform in ϕ and increases near the beam pipe, both features expected from physical signal. Since there is no obvious problem with this distribution, we use the cut proposed in FSQ-16-

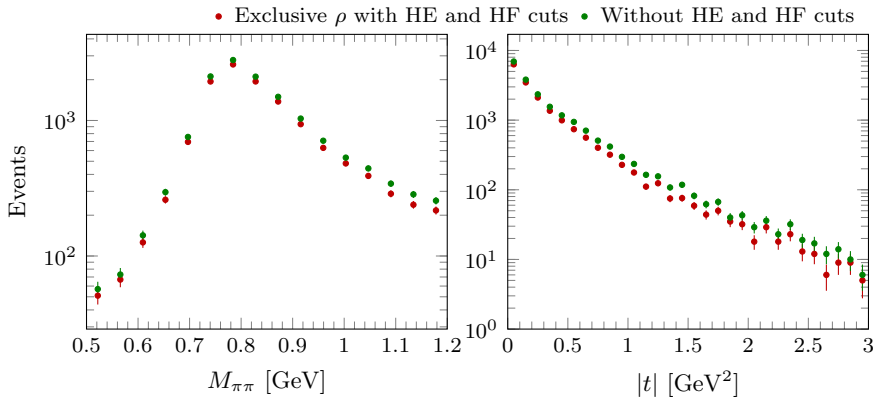

Figure 3.14: Effect of the HE and HF cuts. All exclusivity cuts defined in the present chapter are applied, except for the HE and HF ones.

007.

Because of time constraints, we payed even less attention to the forward hadronic calorimeters HF, and blindly followed the prescriptions from FSQ-16-007. Events with energy deposits $E_{\mathrm{HF}} > 3\,\mathrm{GeV}$ are removed from the considered sample.

The effect of the endcaps cuts on the ρ kinematic distributions is shown on figure 3.14. One can see that a larger proportion of events is removed outside of the mass peak, and that the t shape of the distribution changes slightly, in a way expected for background reduction. There is therefore no obvious reason not to trust the cuts.

3.6 Forward detectors

Our cuts on CASTOR and ZDC are also guided by FSQ-16-007. Following its authors, we require that the energy deposits be under 500 GeV in ZDC− (proton direction) and 2 000 GeV in ZDC+ (lead direction). We use a higher threshold than FSQ-16-007 for CASTOR: 9 GeV instead of 4 GeV.

Figure 3.15 compares the $|t|$ and rapidity distributions of events rejected by the forward calorimeters to our exclusive ρ sample. The asymmetry of CASTOR is clearly visible on the rapidity distribution. It has been accounted for by reweighting events rejected by CASTOR only.

The high-$|t|$ behavior of events rejected by ZDC and CASTOR when in the proton direction is compatible with that of the exclusive ρ sample. The cuts therefore reject part of the contributions to the high-$|t|$ queue of the distribution. This will be important in the next chapter.

3.7 Summary

Let's summarize our most important cuts. We select events with exactly two tracks, of opposite sign and with $|\eta| < 2.4$. One of them must have a p_t above 400 MeV, the other above 250 MeV. The $\phi \to K^+K^-$ background is rejected by requiring $M_{KK} > 1.04\,\mathrm{GeV}$.

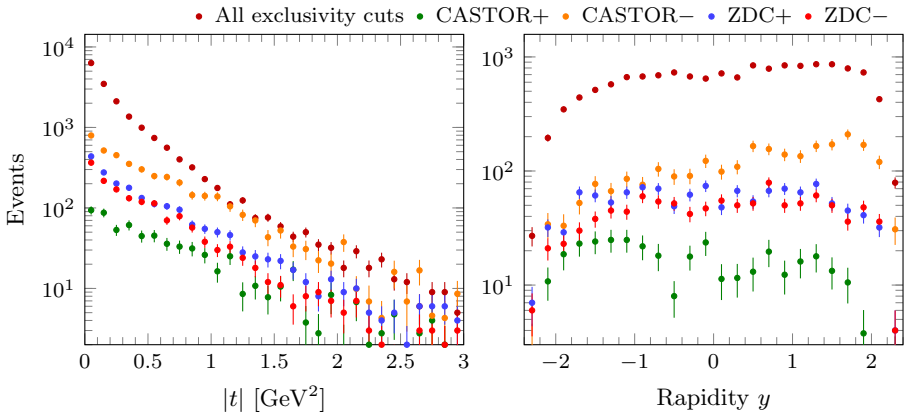

Figure 3.15: $|t|$ and y distributions of events with energy deposits in forward detectors. All cuts on central detectors have been applied (ECAL, HCAL, tracks); events are reweighted to take the CASTOR asymmetry into account. In the plots above, CASTOR+ corresponds to events with CASTOR in the direction taken by the lead ion, and CASTOR− to events with CASTOR in the direction taken by the proton beam.

We were able to use the energy deposit in the ECAL barrel as an exclusivity criterion after removing hot cells. We showed that cutting on the HCAL is in our case not useful. We started a study of the ECAL endcaps, but couldn't finish it due to time constraints.

We used the cuts from FSQ-16-007 for most other detectors: HE, HF and ZDC. We found no obvious reason not to trust them. We use a higher cut on CASTOR, 9 GeV instead of 4 GeV.

3.8 Simulated samples

In addition to the events from CMS, we use two samples of simulated events, which will be used to describe exclusive ρ and ρ' photoproductions. The events were generated using STARlight, then passed through a detailed simulation of the CMS detector. The simulation files include two description levels: the particles thrown in the detector ("generated" level) and the signal from the detector ("reconstructed" level).

We perform the same analysis on simulated samples and on real world data, with the notable exception of the EB cut, because the simulated files don't have enough information to implement it. We don't expect this difference to have a significant impact on our results.

ρ sample

The ρ sample is made of 100 000 diffractive ρ events produced using STARlight. Interference with direct $\pi^+\pi^-$ production is included, using $A = 2.75$ and $B = 1.84\,\text{GeV}^{-1/2}$ in the Söding formula (1.6). The parameters σ_M, η, $\sigma_{\mathbb{P}}$ and ϵ in equation (1.3) are fixed to 26.0 µb, 1.23, 5.0 µb and 0.22 respectively, with the photon-proton center-of-mass energy W expressed in GeV. Other

parameters are fixed to their PDG values [4]. The STARlight description of exclusive ρ photoproduction was tuned to match H1 and ZEUS measurements.

The only ρ decay channel simulated by STARlight is $\rho^0 \to \pi^+\pi^-$. The associated branching ratio is taken to be 100 %, which is very close to its actual value. STARlight assumes that the ρ inherits its helicity from the photon (a feature known as s-channel helicity conservation, SCHC). Since the amount of longitudinal photons is negligible at high energy, the helicity is always taken to be $\lambda_\rho = \pm 1$. The angular distribution of the final state takes this into account.

ρ' sample

STARlight was also used to produce 100 000 diffractive ρ' events. This channel was primarily developed in STARlight in order to enable studies of the $2(\pi^+\pi^-)$ final state. It is not supposed to describe the ρ' accurately. It could nevertheless be useful to describe 4π events with two pions outside of the acceptance – a background that had to be taken into account in the H1 experiment [17].

STARlight assumes that the values of σ_M, η, $\sigma_{\mathbb{P}}$ and ϵ used for the ρ are also valid for the ρ'. Despite the existence of two overlapping resonance $\rho(1450)$ and $\rho(1700)$, STARlight uses a single Breit-Wigner with a mass $M_{\rho'} = 1540\,\text{MeV}$ and a width $\Gamma_{\rho'} = 570\,\text{MeV}$. The decay is simulated using a phase-space distribution (i.e. the angular distribution is flat). This description matches the STAR observations.

Limitations

The two Monte-Carlo samples have some limitations that may affect our analysis, and in particular the t slope of the cross section.

The main issue is the lack of a sample describing proton dissociation. Its cross section is lower than in the elastic case, but also has a lower t slope, and is therefore dominant at high $|t|$. We'll handle this background using a data-driven approach that, as we shall see, leads to large systematic uncertainties. A proton-dissociative sample could help reducing them.

Since our analysis relies on stringent cuts on all subdetectors, taking noise and pileup into account is very important. The noise generated by the detector simulation can be different from the real one, an obvious example being hot cells (they are absent from the simulations). This could be handled by superimposing zero-bias events on top of the simulated detector response, which would take both noise and pileup into account. This isn't done in this analysis.

Chapter 4

Extraction of the cross section

As discussed in the previous chapter, we use the detector to the best of its capabilities to reduce backgrounds. With all cuts applied, our event sample is mostly made of exclusive ρ events, but it does also contain remaining contributions from other processes. We still need to take this into account, and convert the number of observed $p\mathrm{Pb} \to \mathrm{Pb}\pi^+\pi^- p$ events to a $\gamma p \to \rho p$ cross section. The extraction of the cross section is done in several steps, that we now discuss briefly.

The first step takes into account the events from proton dissociation not handled by the exclusivity cuts. We evaluate their contribution by fitting a sum of different templates to the data, and substract it from the measured histograms. This will give us distributions that are free of the proton-dissociative component.

The next step in the analysis is to take into account the detector acceptance and efficiency. This is done by applying a procedure called "Bayesian unfolding" to the histograms obtained by substracting the proton-dissociative background. This gives us access to the $\gamma p \to \pi^+\pi^- p$ cross section.

Once we get the $\gamma p \to \pi^+\pi^- p$ cross section, we still have to isolate its resonant part ($\gamma p \to \rho p \pi^+\pi^- p$). We do this by fitting the Söding formula (1.6) to the observed invariant mass distributions, and retaining its purely resonant component only.

We repeat the last two steps of the procedure in various (W, t) bins in order to get measurements of the total averaged cross section, the W-dependence of the cross section and the t-differential cross section. The results are compared to those of H1 and ZEUS at HERA.

4.1 Proton-dissociative background

There is no way to remove the remaining backgrounds on an event-by-event basis. However, if their distributions are known, they can be substracted from the observed distribution to get the signal:

$$[\text{observed}] = [\text{signal}] + \sum_i [\text{background}]_i, \tag{4.1}$$

The square brackets mean that the above equation is a relation between distributions.

In order to substract backgrounds, we must therefore know their distributions and, most importantly, normalize them correctly – else equation (4.1) doesn't hold. A way to estimate the normalizations is to fit a linear combination of "templates" to the observed distribution:

$$[\text{observed}] \overset{\text{fit}}{\equiv} \alpha[\text{signal template}] + \sum_i \alpha_i[\text{background template}]_i.$$

If one can get a good fit for one distribution and the considered background contributions are relevant, all other kinematic distributions should match with the same normalizations.

The distribution used to fit must be chosen carefully. Indeed, if the templates share the same behavior, the result will be meaningless. The obvious candidate is in our case the p_t (or equivalently t) distribution, because the various contributions have different t slopes.

The four templates considered in this analysis are described in the next section. We will then discuss the fit results.

Fitting templates

Our signal template will be given by the ρ simulation. However, since one of the main motivations for this work was the measure of the t slope of the cross section, we need to avoid depending on what STARlight predicts. If we use the STARlight output as is, our results will reflect the STARlight parametrization. In order to suppress this model dependence, we allow for a reweighting of the t slope, $[\rho \text{ signal}] \mapsto e^{-\Delta b p_t^2}[\rho \text{ signal}]$, where Δb is determined by the fitting procedure.

The first background template, describing diffractive production of the $\rho'(\to 4\pi)$ meson, was produced using STARlight as discussed in section 3.8. Consideration was given to normalizing it using three-tracks events, but this was found to be impossible. Indeed, the ρ' simulation can't describe the observed distribution of track multiplicity: the ratio of the number of two-tracks events to the number of three-tracks events is 3:1 in data, while it is 23:1 in the simulation. (Four-pions events can be reconstructed as two- or three-tracks events when one or more pions' p_t is under threshold.)

A third template (called "3π" below) was produced using three-tracks events, and keeping only two of them (we keep the two tracks of opposite sign with $M_{\pi\pi}$ closest to M_ρ). This method is mainly motivated by the bad description of track multiplicity by the ρ' simulation. As we shall see, it turns out that the $|t|$ slope of the 3π template is compatible with the one for exclusive ρ events for $|t| \to \infty$ – where the proton-dissociative background is expected.

A template for proton dissociation ("p-diss") was produced by inverting the cuts on CASTOR and ZDC on the $-z$ side of the detector. Events with hits in CASTOR only are reweighted to take the detector asymmetry into account.

Figure 4.1 shows the t dependence of these four fit templates. The 3π and p-diss templates have the similar asymptotic slopes, but different behaviors below $|t| \simeq 0.7\,\text{GeV}^2$. The ρ and ρ' slopes are clearly different from each other and from the other templates.

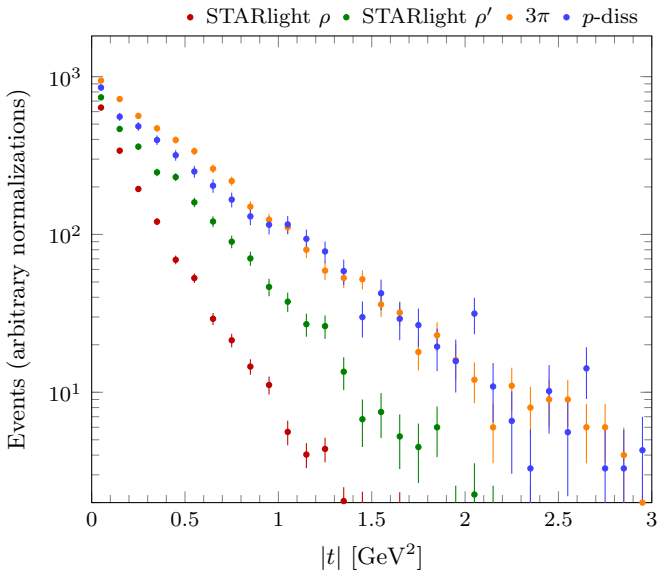

Figure 4.1: t distributions of the four fit templates. The normalizations were chosen to highlight the differences between the templates.

Fit to data

As already mentioned, we fit a linear combination of our four templates to the p_t distribution of events observed in CMS:

$$[\text{observed}]_{p_t} \equiv \alpha_\rho e^{-\Delta b p_t^2} [\rho]_{p_t} + \alpha' [\rho']_{p_t} + \alpha_p [p\text{-diss}]_{p_t} + \alpha_3 [3\pi]_{p_t},$$

where the brackets are there to remind that this is a relation between distributions. The fit parameters are the slope difference Δb and the four normalizations α.

Fitting with all parameters left free leads to two interesting results. First, the ρ' normalization is zero independently of its initial guess. This is unexpected because this contribution was needed at H1 [17]; it is probably included in the 3π template. The second result is that the p-diss and 3π templates are almost 100 % anti-correlated[1]. This is obviously because their asymptotic t slopes are identical.

The strong anti-correlation between the p-diss and 3π templates is an indication that both templates could describe data equally well. Indeed, the fits with $\alpha_p \equiv 0$ or $\alpha_3 \equiv 0$ are equally good, although they lead to different values of Δb: a fit with only p-diss ($\alpha_3 = 0$) leads to $\Delta b = 1.1\,\text{GeV}^{-2}$, and a pure 3π fit ($\alpha_p = 0$) to $\Delta b = 1.9\,\text{GeV}^{-2}$. The results of the fits are listed in table 4.1. Different combinations of the two templates lead to intermediate values of Δb.

The fits results for $\alpha_3 = 0$ (hereafter called the "p-diss" fit) are shown on figure 4.2; the 3π fit ($\alpha_p = 0$) is shown on figure 4.3. The p_t, $|t|$ and rapidity distributions are matched by the templates. The mass peak, on the other hand, isn't reproduced well; this can be caused by a systematic shift in

[1] The signal template is obviously also anti-correlated with each of the backgrounds, but to a smaller extent (less than about 20 %).

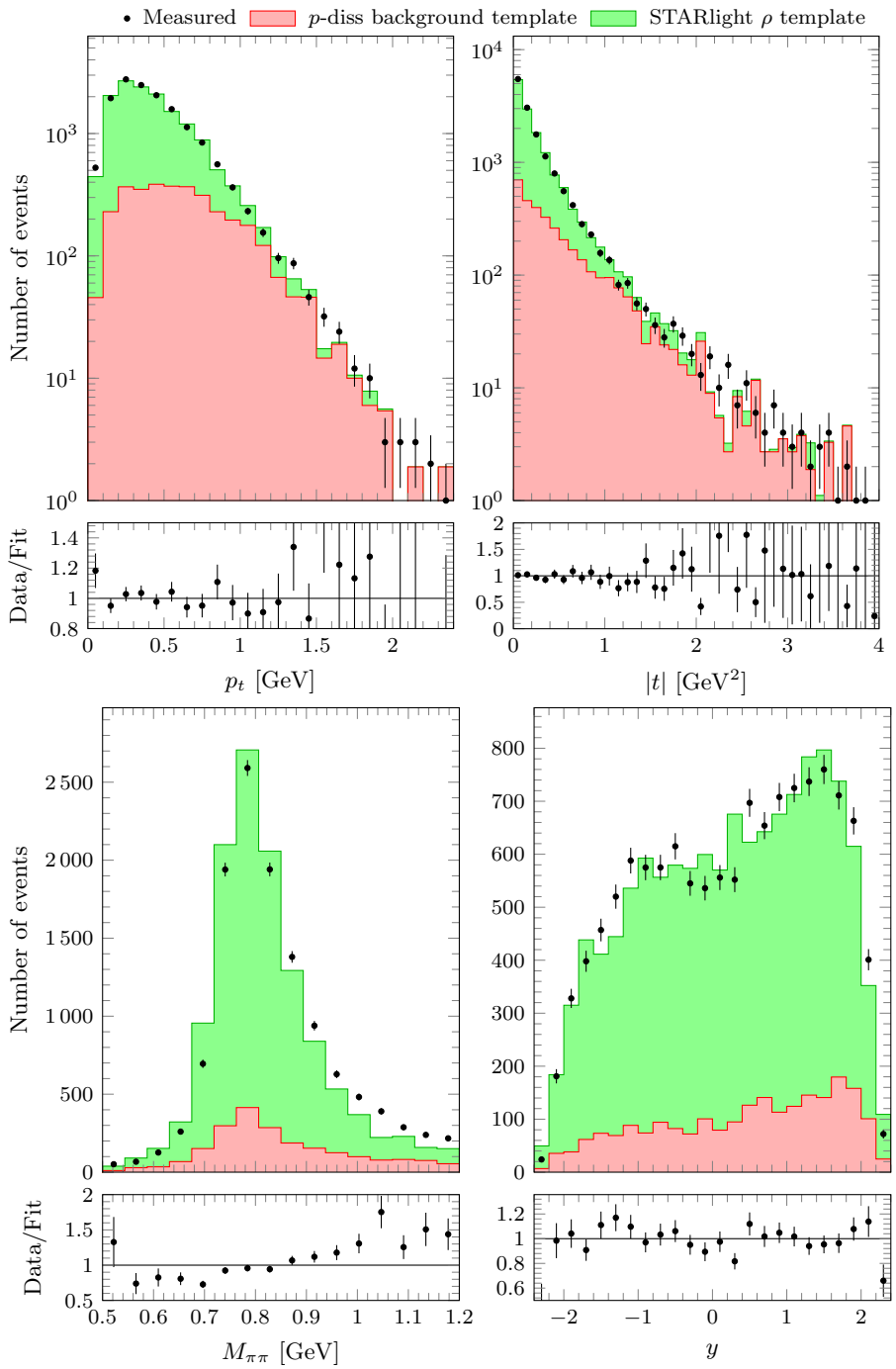

Figure 4.2: Fit results for the p-diss template. The upper part of each plot shows the sum of all contributions compared to data; the ratio of the two is displayed in the lower part. All statistical and fitting errors are included in the ratio plots, except for the ρ template t slope reweighting.

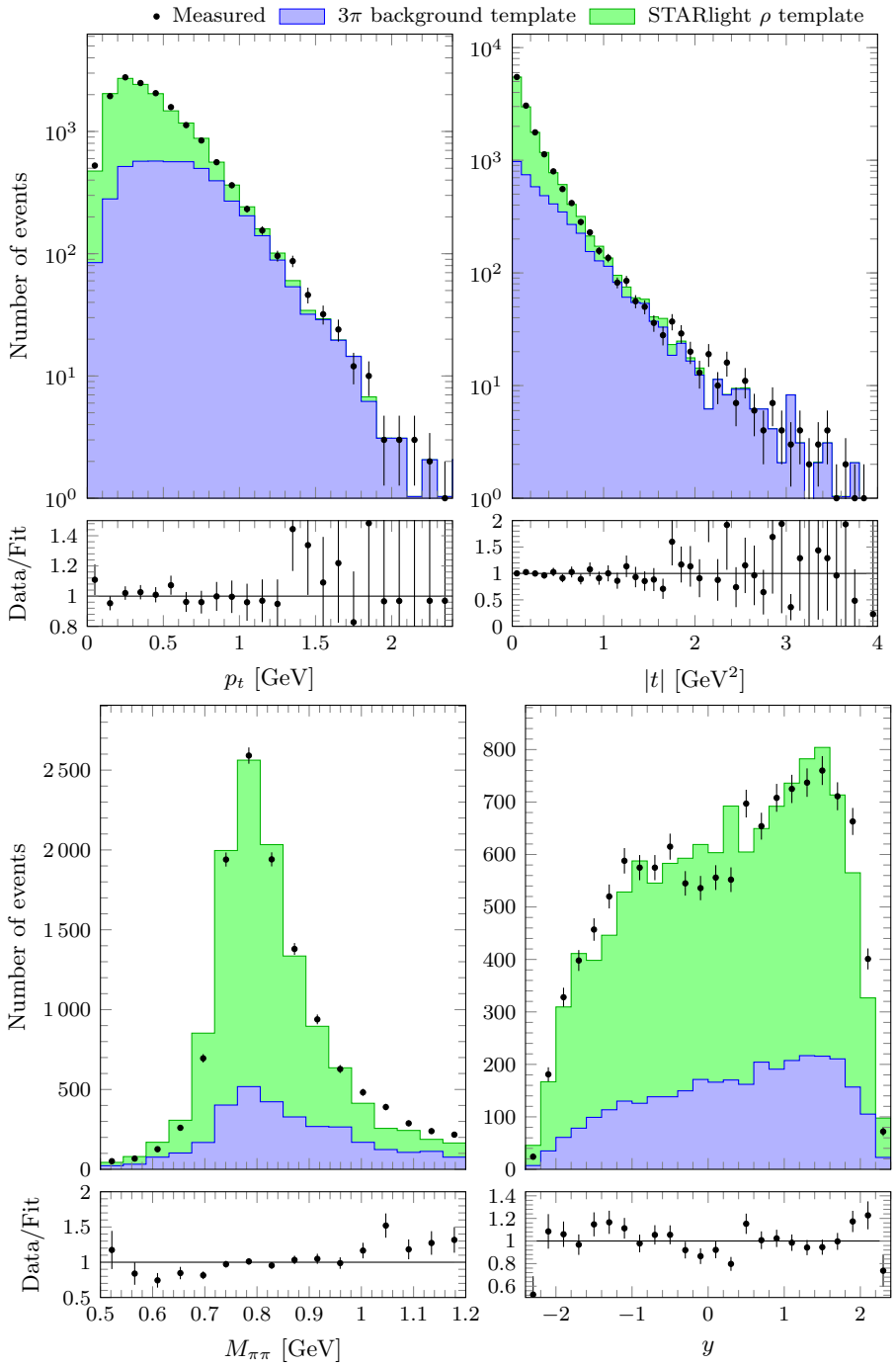

Figure 4.3: Fit results for the 3π template. The upper part of each plot shows the sum of all contributions compared to data; the ratio of the two is displayed in the lower part. All statistical and fitting errors are included in the ratio plots, except for the ρ template t slope reweighting.

Parameter	p-diss fit	3π fit
α_ρ	3.33 ± 0.05	3.29 ± 0.06
Δb [GeV^{-2}]	1.1 ± 0.2	1.9 ± 0.3
α_p	0.8 ± 0.1	–
α_3	–	1.0 ± 0.1
α'	$< 10^{-8}$	$< 10^{-9}$

Table 4.1: Results of the background fits with the 3π and p-diss components set to zero (left and right columns, respectively). The ρ' contribution is in all cases negligible, and the values of Δb aren't compatible.

the reconstruction of low-p_t tracks or a direct $\pi^+\pi^-$ contribution lower than expected. The situation is somewhat better for the 3π fit than for p-diss.

Since the two fits are very close to being good, let's not worry yet about which one to choose. We'll do the analysis for both, and use the difference between them to estimate the systematic uncertainty caused by the choice of template for proton dissociation.

4.2 Evaluation of the cross section

We describe below how we extract the $\gamma p \to \rho p$ cross section from the distributions obtained by substracting the proton-dissociative background. We will first expose the procedure used to take detector effects into account. Once done, we will see how to compute the photon-proton cross section using proton-lead events. We will finish by discussing how we handle the remaining backgrounds, including direct $\pi^+\pi^-$ production.

Acceptance and efficiency

Detectors aren't perfect; so aren't their measurements. Two effects can be considered: migration between histogram bins and missed events. Moreover, particles can be produced outside of the acceptance (i.e. they are undetectable because of the detector geometry). These effects are accounted for using simulations.

In the absence of migration between bins, one can multiply their contents N_i by factors that takes both acceptance and efficiency into account:

$$\hat{N}_i = \frac{1}{\mathcal{A}_i \mathcal{E}_i} N_i,$$

where N_i is the number of detected particles in the bin i (after background substraction), $\hat{N}_i$ is the "true" number of particles, $\mathcal{A}_i$ is the acceptance and $\mathcal{E}_i$ is the detection efficiency.

This is, however, a special case. Correcting for event migration is often needed, especially when measuring sharp distributions, because it has a smoothing effect. Data migration can be modeled as:

$$N_i = \sum_j (\mathcal{E}\mathcal{A})_{ij} \hat{N}_j,$$

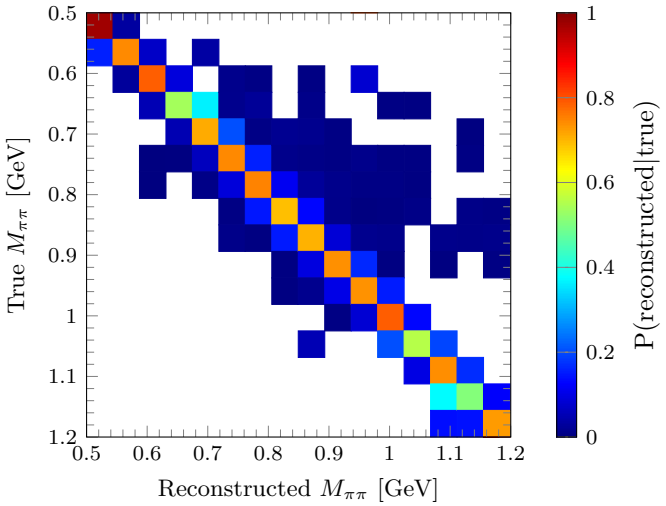

Figure 4.4: Invariant mass response matrix, as evaluated from the ρ simulation. It is mostly diagonal, indicating that the bin width matches the detector resolution. Rows are normalized to unity; white cells correspond to P(reconstructed|true) = 0.

where the $(\mathcal{EA})$ is called the response matrix, and describes both migration, acceptance and efficiency. The matrix element $(\mathcal{EA})_{ij}$ can be interpreted as the probability $\mathrm{P}(i|j)$ for an event in bin j to be measured in bin i.

Inverting the relation above ("unfolding" the measured distribution) is tricky, and simply inverting the response matrix doesn't give good results. We use the method first proposed by d'Agostini [26] (as implemented in `RooUnfold` [27]), based on Bayesian statistics. It describes data migration as a set of causes and consequences, where every consequence can result from any number of causes with known probabilities. Acceptance and efficiency are implemented by adding a consequence for missed events.

Unfolding can be used to account for data migration, but cannot supplement a bad detector resolution. It is therefore important to check that the bins are larger than the detector resolution. This can be checked by looking at the response matrix: if it is mostly diagonal, we are safe. The response matrix for the invariant mass $M_{\pi\pi}$ is represented on figure 4.4.

We unfold the signal distributions obtained by inverting equation (4.1):

$$[\text{signal}] = [\text{observed}] - \sum_i [\text{background}]_i.$$

This gives us the "true" distributions of events, fully corrected for acceptance, efficiency and data migration.

Cross section calculation

Extracting a photon-proton cross section from proton-lead events isn't trivial. In this section, we expose the procedure followed to compute the $\gamma p \to p\pi^+\pi^-$ cross sections.

The elementary proton-lead cross section $\mathrm{d}\sigma_{\mathrm{Pb}p\to\mathrm{Pb}p\pi^+\pi^-}$ associated with one measured $\pi^+\pi^-$ event can be found using the integrated luminosity $\mathcal{L}$:

$$\mathrm{d}\sigma_{\mathrm{Pb}p\to\mathrm{Pb}p\pi^+\pi^-} = \frac{1}{\mathcal{L}}\frac{1}{\mathcal{AE}},$$

where we neglected migration between bins. Integrating this relation with respect to the kinematics of the final state gives the proton-lead cross section for $\pi^+\pi^-$ production:

$$\sigma_{\mathrm{Pb}p\to\mathrm{Pb}p\pi^+\pi^-} = \frac{\hat{N}_{\pi^+\pi^-}}{\mathcal{L}},$$

where $\hat{N}_{\pi^+\pi^-}$ is the "true" number of events with a $\pi^+\pi^-$ final state.

In order to compute the photon-proton cross section, one needs the photon-proton cross section element $\mathrm{d}\sigma_{\gamma p\to p\pi^+\pi^-}$. For an event e, it can be computed from from $\mathrm{d}\sigma_{\mathrm{Pb}p\to\mathrm{Pb}p\pi^+\pi^-}$ using the photon flux Γ (see section 1.4):

$$\mathrm{d}\sigma_{\gamma p\to p\pi^+\pi^-}(W_e) = \frac{1}{\Gamma(W_e)}\mathrm{d}\sigma_{\mathrm{Pb}p\to\mathrm{Pb}p\pi^+\pi^-} = \frac{1}{\mathcal{L}}\frac{1}{\mathcal{AE}}\frac{1}{\Gamma(W_e)},$$

where W_e is the measured photon-proton center-of-mass energy. Integrating on the final state kinematics and averaging on the interval $\mathscr{I} \equiv [W, W+\Delta W]$, one gets:

$$\langle\sigma_{\gamma p\to p\pi^+\pi^-}\rangle_{\mathscr{I}} = \frac{1}{\Delta W}\frac{1}{\mathcal{L}}\frac{1}{\mathcal{AE}}\sum_{e|W_e\in\mathscr{I}}\frac{1}{\Gamma(W_e)} \equiv \frac{1}{\Delta W}\frac{\hat{\mathcal{N}}^{\mathscr{I}}_{\pi^+\pi^-}}{\mathcal{L}}, \tag{4.2}$$

where we'll call $\hat{\mathcal{N}}^{\mathscr{I}}_{\pi^+\pi^-}$ the "equivalent number of events" and has the dimension of an energy. The generalization of this relation in order to take data migration into account is straightforward.

The expression for a differential cross section is obtained by integrating on a small subset $\square$ of the final state phase space (e.g. an histogram bin). For example, if $\square = [t, t+\Delta t]$ is a small interval in t, one gets:

$$\left\langle\frac{\mathrm{d}\sigma_{\gamma p\to p\pi^+\pi^-}}{\mathrm{d}t}(t)\right\rangle_{\mathscr{I}} \approx \frac{1}{\Delta W}\frac{1}{\Delta t}\frac{1}{\mathcal{L}}\frac{1}{\mathcal{AE}}\sum_{e|W_e\in\mathscr{I},t_e\in\square}\frac{1}{\Gamma(W_e)}.$$

Further corrections can be applied to account for the variation of the differential cross section; we won't do it here.

Suppression of the residual backgrounds

Before we can use equation (4.2) to compute the cross section, we have to estimate the remaining background contributions. The most important one is direct $\pi^+\pi^-$ production, including its interference with the ρ. The other non-negligible contributions come from the production of the ϕ and ω vector mesons.

We'll take the direct $\pi^+\pi^-$ background into account by fitting invariant mass distributions to the Söding formula (see section 1.3):

$$\frac{\mathrm{d}\sigma_{\gamma p\to p\pi^+\pi^-}}{\mathrm{d}M_{\pi\pi}} \propto \left|A\frac{\sqrt{M_{\pi\pi}M_\rho\Gamma(M_{\pi\pi})}}{M^2_{\pi\pi}-M^2_\rho+iM_\rho\Gamma_\rho(M_{\pi\pi})} - B\right|^2.$$

We will then integrate the Breit-Wigner part of the cross section in the full mass range:

$$\sigma_{\gamma p\to\rho p} \propto \int_{2m_\pi}^{\infty} \mathrm{d}M_{\pi\pi} \left| A\frac{\sqrt{M_{\pi\pi}M_\rho\Gamma(M_{\pi\pi})}}{M_{\pi\pi}^2 - M_\rho^2 + iM_\rho\Gamma_\rho(M_{\pi\pi})}\right|^2 = 2.02294\,|A|^2. \quad (4.3)$$

Another non-negligible background comes from the $\omega \to \pi^+\pi^-$ decay. At the typical values of W studied here, the ω cross section is small ($\sigma_\rho/\sigma_\omega \sim 10$), and so is the branching ratio of the $\omega \to \pi^+\pi^-$ decay (1.5 %). However, the ω-ρ interference term isn't negligible and increases the $\pi^+\pi^-$ cross section by about 4 % in the range $0.5 < M_{\pi\pi} < 1.2\,\mathrm{GeV}$ [16]. We'll scale the cross section by 96 %.

The last background comes from the three-pions decays $\omega \to \pi^+\pi^-\pi^0$ and $\phi \to \pi^+\pi^-\pi^0$. Due to the presence of a third pion, these contributions show up at high $|t|$ and low invariant mass, mostly below $M_{\pi\pi} < 0.65\,\mathrm{GeV}$ [16]. Part of their contribution may already have been accounted for by the p_t fit. We will nevertheless ignore the low invariant mass region for the mass fits.

In order to limit the uncertainty due to background removal, we restrain the data taken into account for the fit to the range $|y| < 2.1$ and $|t| < 0.5\,\mathrm{GeV}^2$.

We will keep the ρ and $\pi^\pm$ masses fixed to their PDG values [4]; A, B and Γ_ρ will be left free.

4.3 Averaged cross section

In this section, we evaluate the averaged cross section on the full W range. As described above, we fit Söding formula to the invariant mass distribution $\mathrm{d}\hat{\mathcal{N}}/\mathrm{d}M_{\pi\pi}$. We sum on events covering the whole W domain accessible to CMS ($30 < W < 250\,\mathrm{GeV}$, with a flux-corrected average $\langle W\rangle_\Gamma = 141\,\mathrm{GeV}$).

The invariant mass fits using the p-diss and 3π background templates are shown on figures 4.5 and 4.6. The errors on the data points come from the statistics, the error on the normalization of the proton-dissociative background templates, and the unfolding procedure. Given that we had to multiply the simulated signal by three to match the data, the last contribution is likely dominant.

One can be scared of the big χ^2's, but they mostly come from the region $0.9 < M_{\pi\pi} < 1.2\,\mathrm{GeV}$, i.e. from outside of the peak. The values of the ρ width Γ_ρ found by the fits are compatible with its PDG value of 149 MeV.

The value of A is stable when changing the fit bounds and the binning, but B is not. In particular, B is very sensitive to the upper bound of the fit. We didn't have the time to look at these effects in detail, and won't rely on the values of B and B/A in the following.

The $\gamma p \to \rho p$ cross section can be calculated from equation (4.3), keeping in mind that it is a W average and substracting the ω-ρ interference term:

$$\langle\sigma_{\gamma p\to\rho p}\rangle = 96\,\%\frac{1}{\Delta W}\frac{1}{\mathcal{L}}\,2.02294\,|A|^2.$$

Before computing the cross section, let's take a look at the systematic uncertainties.

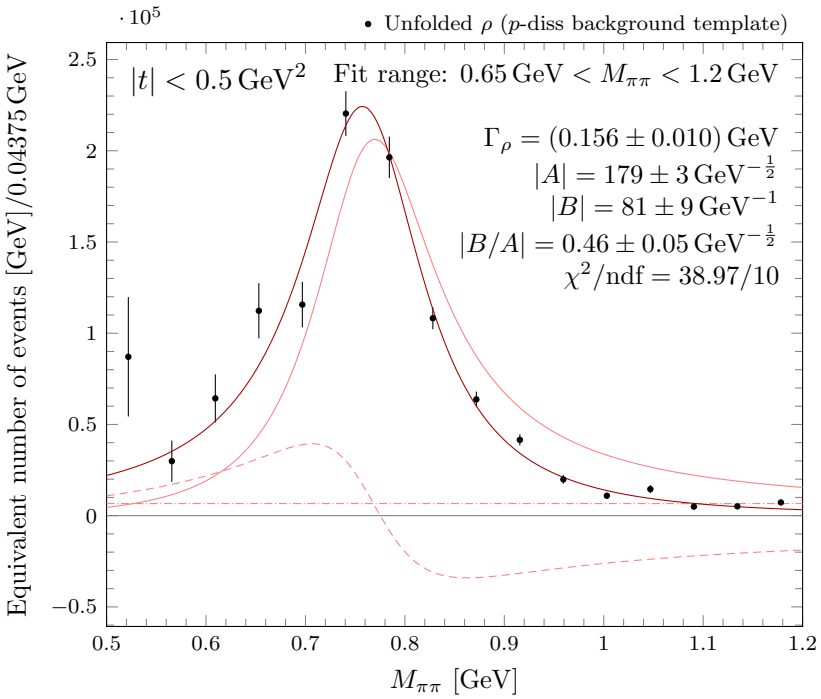

Figure 4.5: Fit of the invariant mass distribution for the p-diss background template. The dark curve is the fit to the Söding formula. The light solid curve is the Breit-Wigner term, the dashed one is the interference, and the dot-dashed line is the direct $\pi^+\pi^-$ background.

Systematic uncertainties

Systematic uncertainties in this analysis come from several sources, from track reconstruction to the modeling of the mass peak. They need to be estimated in order to get meaningful results.

The authors of FSQ-16-007 use the estimation of the uncertainty due to track reconstruction efficiency from another analysis, FSQ-12-004, that found 7.8 %. Concerning the exclusivity cut, they studied the effect of varying the cuts on CASTOR and HF by 17 % and 5 % respectively, and found an uncertainty of 1.4 %. For the uncertainty on the fit procedure, they used a plain Breit-Wigner distribution instead of the Söding formula, and found a variation of 5 %. The dependence on the flux calculation was estimated to 5 %. As we didn't have the time to estimate these uncertainties, we use the values above.

We already saw in chapter 3 that the value of the luminosity $\mathcal{L}$ is known to 3.6 %. We estimate the uncertainty on the ω-ρ interference term by varying the $\sigma_{\gamma p \to \omega p}$ exclusive cross section by 30 %, because it isn't well measured above $W = 20\,\mathrm{GeV}$. This corresponds to a relative error of 15 % on the interference term.

We didn't have the time to estimate the error due to the mass binning and, most importantly, to the fit bounds. Their impact on the ρ cross section is expected to be marginal, but they do affect the evaluation of the direct $\pi^+\pi^-$ cross section.

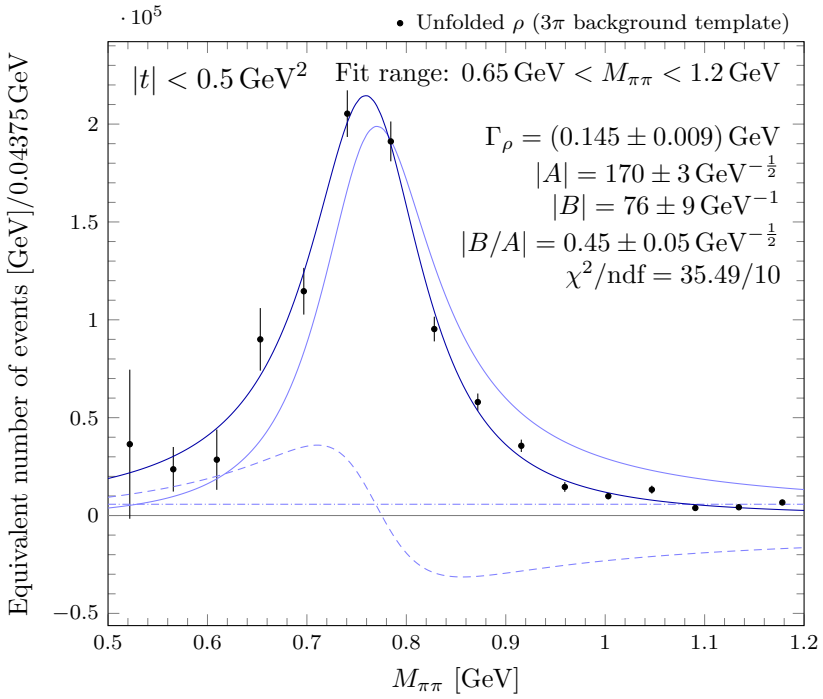

Figure 4.6: Fit of the invariant mass distribution for the 3π background template. The dark curve is the fit to the Söding formula. The light solid curve is the Breit-Wigner term, the dashed one is the interference, and the dot-dashed line is the direct $\pi^+\pi^-$ background.

Source	$\Delta\sigma/\sigma$	Method
Luminosity	3.6 %	[25]
Exclusivity criteria*	1.4 %	Varying CASTOR and HF cuts
Track reconstruction*	7.8 %	FSQ-12-004
t binning, Söding formula*	5 %	Variation of the t binning and fits using a plain Breit-Wigner
Flux calculation*	5 %	
ω-ρ interference	0.6 %	Variate $\sigma_{\gamma p \to \omega p}$ by 50 %
$M_{\pi\pi}$ binning and fit bounds	?	No evaluation

Table 4.2: Estimated systematic uncertainties, except dependence on the background template for proton dissociation. Values for starred sources are taken from FSQ-16-007.

W [GeV^2]		$\langle\sigma\rangle$ [μb]			$\Delta\langle\sigma\rangle$ [μb]		
From	To	p-diss	3π	avg	p-diss	3π	avg
30	50	7.7	6.7	7.2	0.9	0.8	1.0
50	64	11.8	11.5	11.6	1.5	1.4	1.5
64	80	10.5	9.6	10.0	1.3	1.2	1.3
80	110	11.6	9.7	10.6	1.4	1.2	1.6
110	170	15.4	14.5	15.0	1.8	1.7	1.8
170	250	17.7	17.3	17.5	2.2	2.2	2.2

Table 4.3: Values of the $\gamma p \to \rho p$ cross section as a function of W. The "p-diss" and "3π" columns use the p-diss and 3π templates for proton dissociation, respectively. The final estimate is in the "avg" columns.

Table 4.2 summarizes the systematics and their evaluated values. The uncertainty on background subtraction using the p_t fit will be estimated below.

Final results

The cross sections found using the p-diss and 3π background templates are compatible:

$$\langle\sigma^{p\text{-diss}}_{\gamma p\to\rho p}\rangle\Big|_{|t|<0.5\text{ GeV}^2} = 16.6 \pm 0.6(\text{stat.}) \pm 1.9(\text{syst.})\ \mu\text{b}$$
$$\langle\sigma^{3\pi}_{\gamma p\to\rho p}\rangle\Big|_{|t|<0.5\text{ GeV}^2} = 15.0 \pm 0.5(\text{stat.}) \pm 1.7(\text{syst.})\ \mu\text{b}$$

We take their mean and add a systematic error of half their difference for the choice of the background templates, which gives us the final result at $\langle W\rangle_\Gamma = 141\,\text{GeV}$ (integrated on $0 < t < 0.5\,\text{GeV}^2$):

$$\langle\sigma_{\gamma p\to\rho p}\rangle\Big|_{|t|<0.5\text{ GeV}^2} = 15.8 \pm 0.5(\text{stat.}) \pm 2.0(\text{syst.})\ \mu\text{b}.$$

This result is compatible with what was found in FSQ-16-007 (since this analysis isn't public yet, we can't write their result here).

4.4 W dependence of the cross section

We now set out to evaluate the W dependence of the cross section. We proceed exactly as above, except that we restrict our average to smaller W ranges. We keep both M_ρ, Γ_ρ and m_π fixed to their PDG values for fitting, and keep the same estimations of the systematics, including for the background template for proton dissociation. We didn't evaluate the uncertainty due to the choice of the W binning.

The invariant mass fits for both background templates are shown on figures 4.7 and 4.8. The computed cross sections are listed in table 4.3, and compared to the results of past experiments on figure 4.9. Considering the large uncertainties, our points are in agreement with those from H1 and ZEUS.

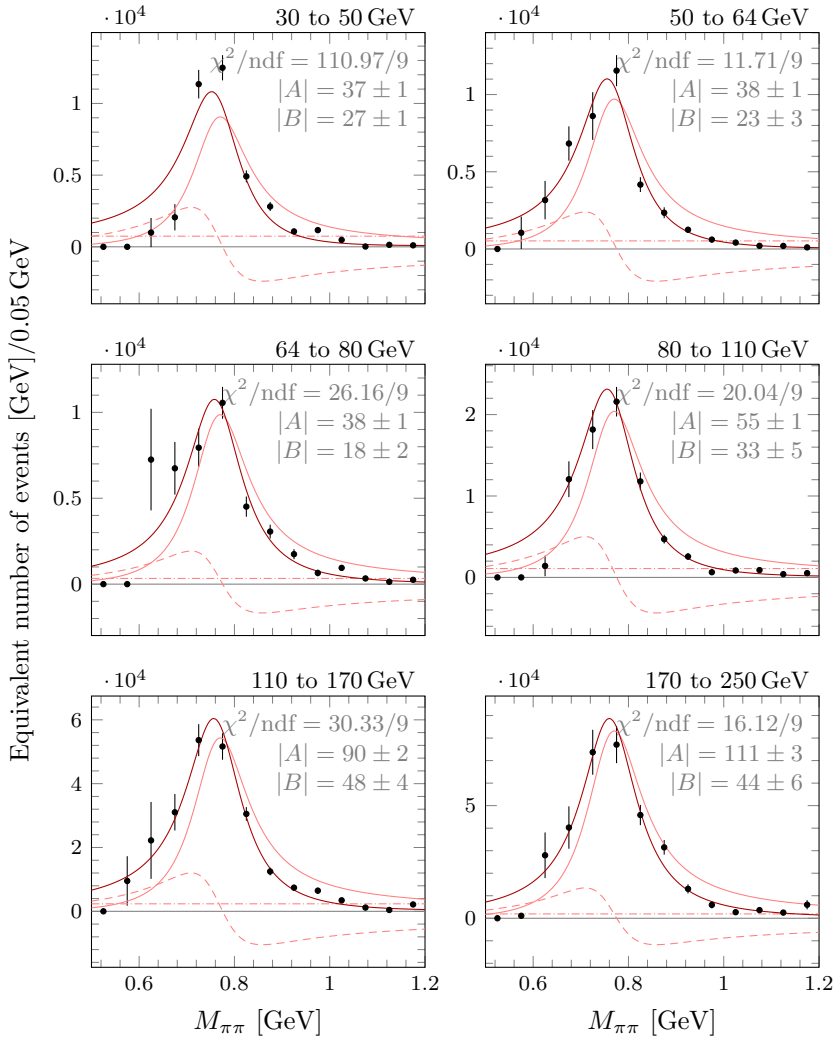

Figure 4.7: Fits of the invariant mass distributions for the p-diss background template, in W bins. The fits are performed in the range $0.65 < M_{\pi\pi} < 1.2\,\text{GeV}$. The black data points are unfolded data. The dark curve is the fit to the Söding formula. The light solid curve is the Breit-Wigner term, the dashed one is the interference, and the dot-dashed line is the direct $\pi^+\pi^-$ background. A and B are given in $\text{GeV}^{-1/2}$ and GeV^{-1}, respectively.

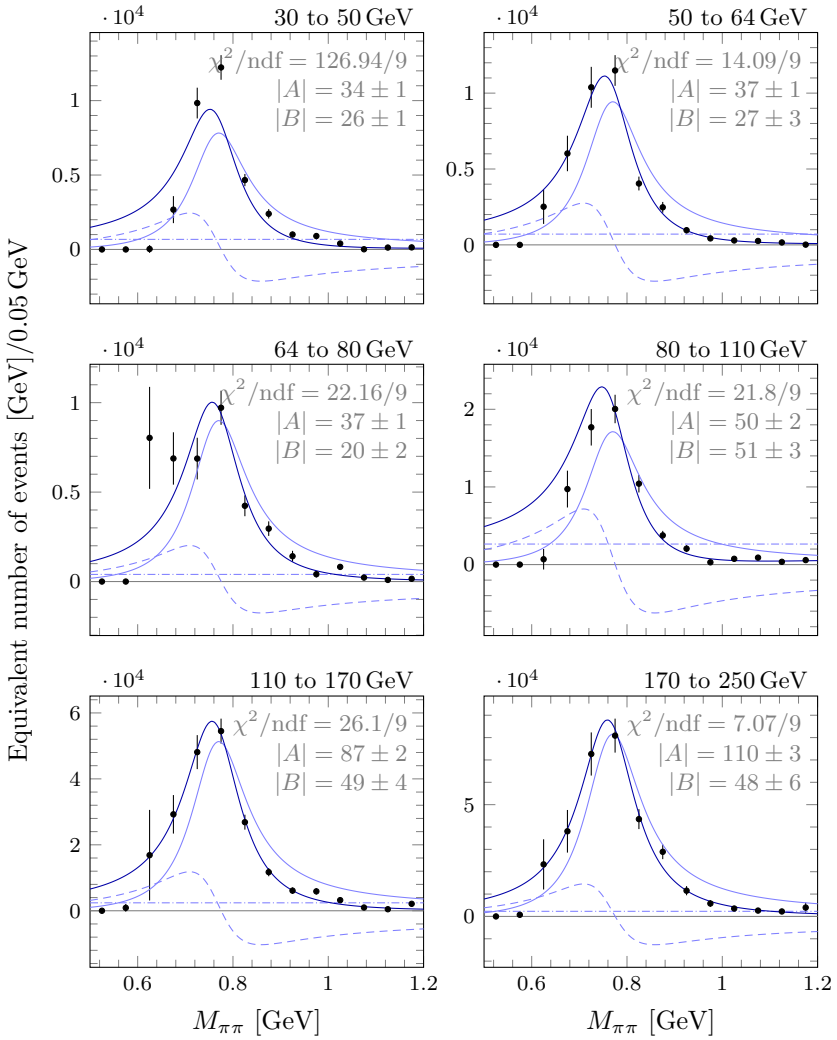

Figure 4.8: Fits of the invariant mass distributions for the 3π background template, in W bins. The fits are performed in the range $0.65 < M_{\pi\pi} < 1.2\,\text{GeV}$. The black data points are unfolded data. The dark curve is the fit to the Söding formula. The light solid curve is the Breit-Wigner term, the dashed one is the interference, and the dot-dashed line is the direct $\pi^+\pi^-$ background. A and B are given in $\text{GeV}^{-1/2}$ and GeV^{-1}, respectively.

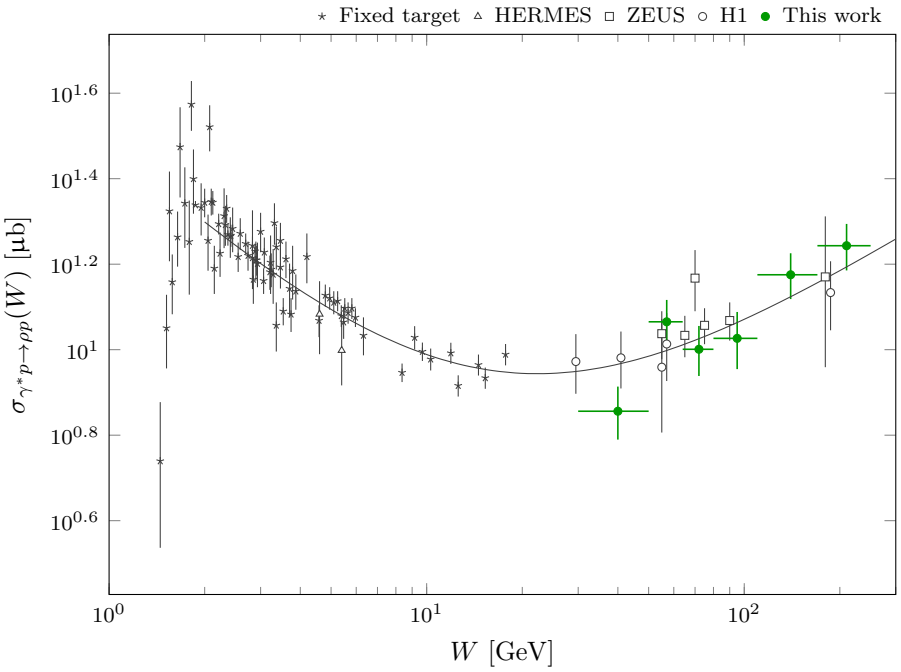

Figure 4.9: Comparison of our measurement of $\sigma_{\gamma p \to \rho p}(W)$ with the results of past experiments. The solid line is a fit of equation (1.7), and doesn't take our points into account. The data was kindly provided by the authors of [10].

4.5 t-differential cross section

We evaluate the t-differential cross section $\mathrm{d}\sigma_{\gamma p \to \rho p}/\mathrm{d}t$ by averaging the t distribution of events on the full W range (as above, $\langle W \rangle_\Gamma = 141\,\mathrm{GeV}$). We use 7 bins in t, covering the range $|t| = 0.025$ to $0.5\,\mathrm{GeV}^2$. As above, the only fit parameters left free are A and B.

The invariant mass fits are shown on figure 4.10 for the p-diss fit and figure 4.11 for the 3π template. Since the fit for the highest-$|t|$ bin using the 3π template didn't converge, we exclude that point.

The systematic uncertainty due to the choice of the background template is evaluated by fitting an exponential to the t distribution for each template, and taking half of the difference between the two fits. This procedure regularizes our estimate with respect to fluctuations of the measured values, in particular at large $|t|$. The fits to data from the two templates are shown on figure 4.12. The t slopes are $b_{p\text{-diss}} = 7.9\,\mathrm{GeV}^2$ and $b_{3pi} = 9.7\,\mathrm{GeV}^2$.

Our estimates for the differential cross section are given in table 4.4, and compared to H1 [14] and ZEUS [15] data on figure 4.13. Our points are in good agreement with the ZEUS measurement, and in tension with what was found at H1.

We find no dip in the t-differential cross section. This is not unexpected, because their predicted location was around $|t| \sim 0.5\,\mathrm{GeV}^2$ for $W = 1\,\mathrm{TeV}$. Since our measurement is at $\langle W \rangle_\Gamma = 141\,\mathrm{GeV}$, the dips would have migrated to even higher $|t|$ (see the end of section 1.2).

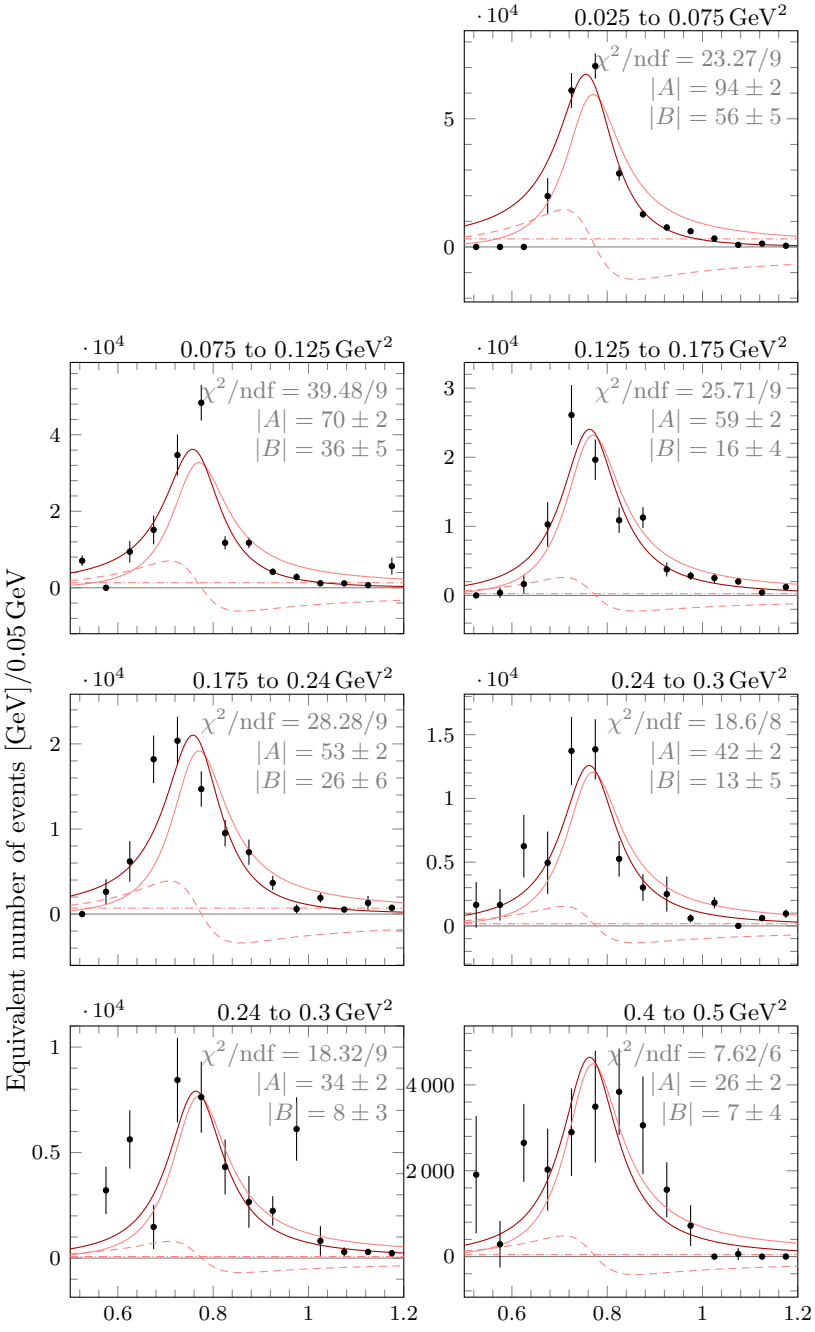

Figure 4.10: Fits of the invariant mass distribution for the p-diss background template, in $|t|$ bins. The black data points are unfolded data. The dark curve is the fit to the Söding formula. The light solid curve is the Breit-Wigner term, the dashed one is the interference, and the dot-dashed line is the direct $\pi^+\pi^-$ background. A and B are given in $\mathrm{GeV}^{-1/2}$ and GeV^{-1}, respectively.

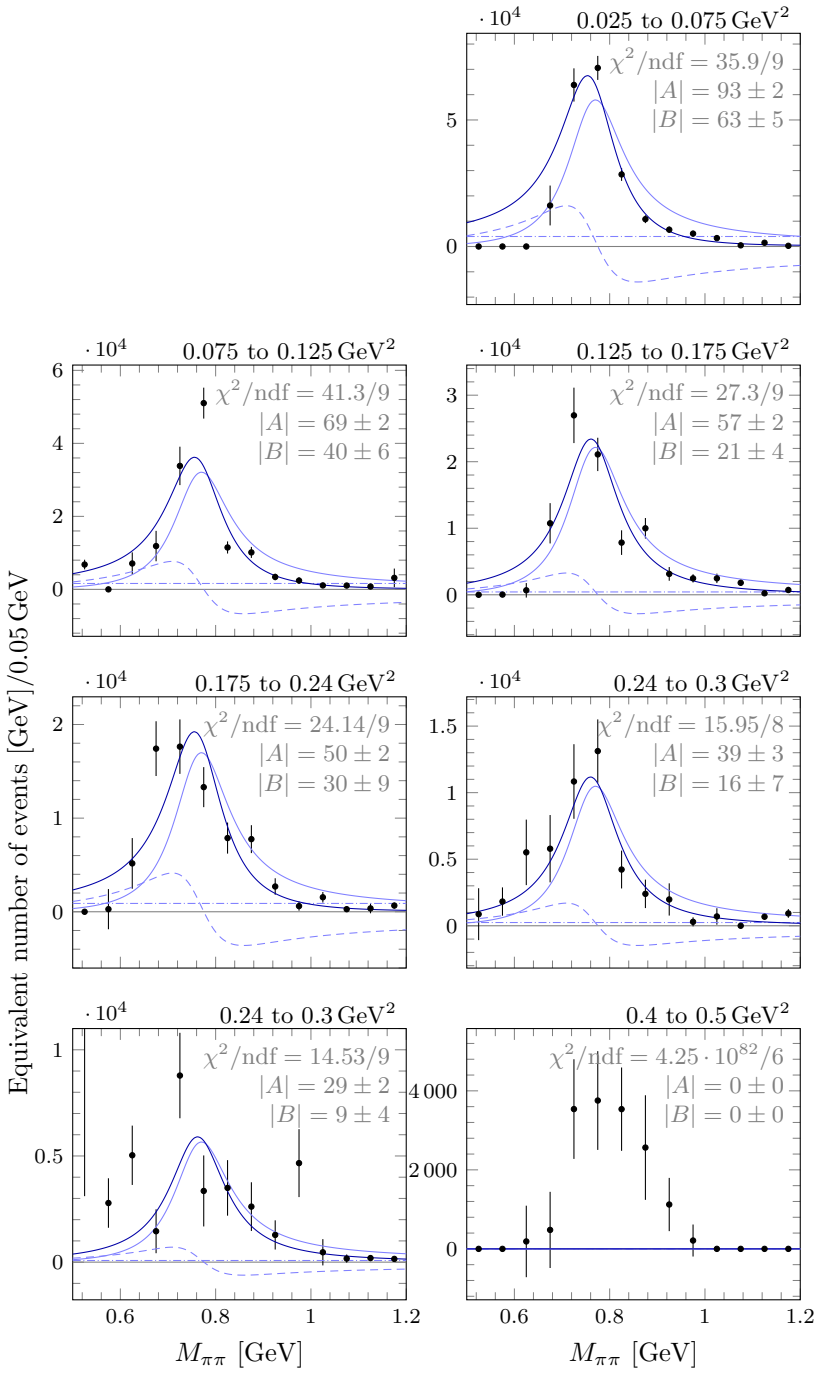

Figure 4.11: Fits of the invariant mass distribution for the 3π background template, in $|t|$ bins. The black data points are unfolded data. The dark curve is the fit to the Söding formula. The light solid curve is the Breit-Wigner term, the dashed one is the interference, and the dot-dashed line is the direct $\pi^+\pi^-$ background. A and B are given in $\text{GeV}^{-1/2}$ and GeV^{-1}, respectively.

$\lvert t\rvert$ [GeV^2]		$\langle \frac{d\sigma}{d\lvert t\rvert} \rangle \left[\frac{\mu b}{GeV^2}\right]$			$\Delta\langle \frac{d\sigma}{d\lvert t\rvert} \rangle \left[\frac{\mu b}{GeV^2}\right]$		
From	To	p-diss	3π	avg	p-diss	3π	avg
0.025	0.075	92	90	91	11	11	11
0.075	0.125	51	50	50	7	6	7
0.125	0.175	36	34	35	5	5	5
0.175	0.240	23	20	22	3	3	4
0.240	0.300	16	14	15	2	2	3
0.300	0.400	6	4	5	1	1	2
0.400	0.500	4	-	4	1	-	2

Table 4.4: Values of the t-differential $\gamma p \to \rho p$ cross section. The "p-diss" and "3π" columns use the p-diss and 3π templates for proton dissociation, respectively. The final estimate is in the "avg" columns.

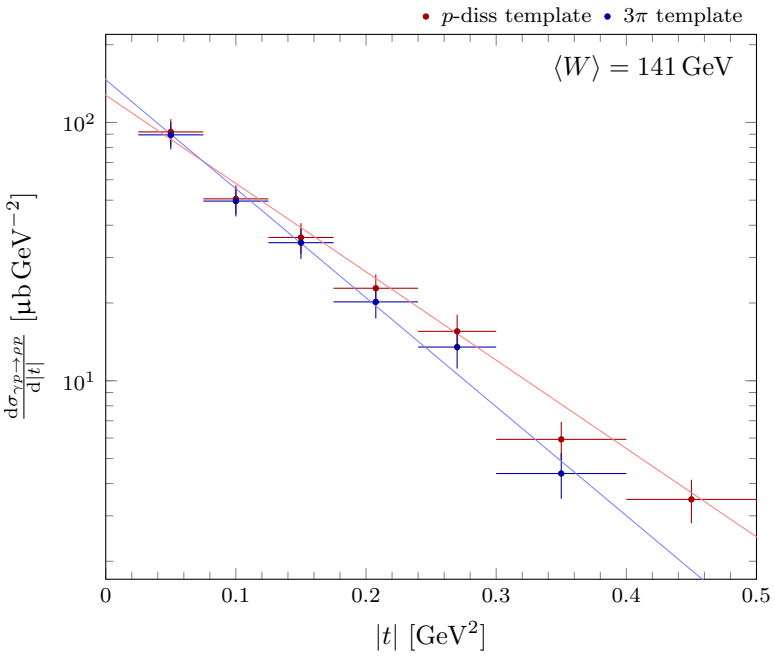

Figure 4.12: Exponential fits to the t distributions for two background templates.

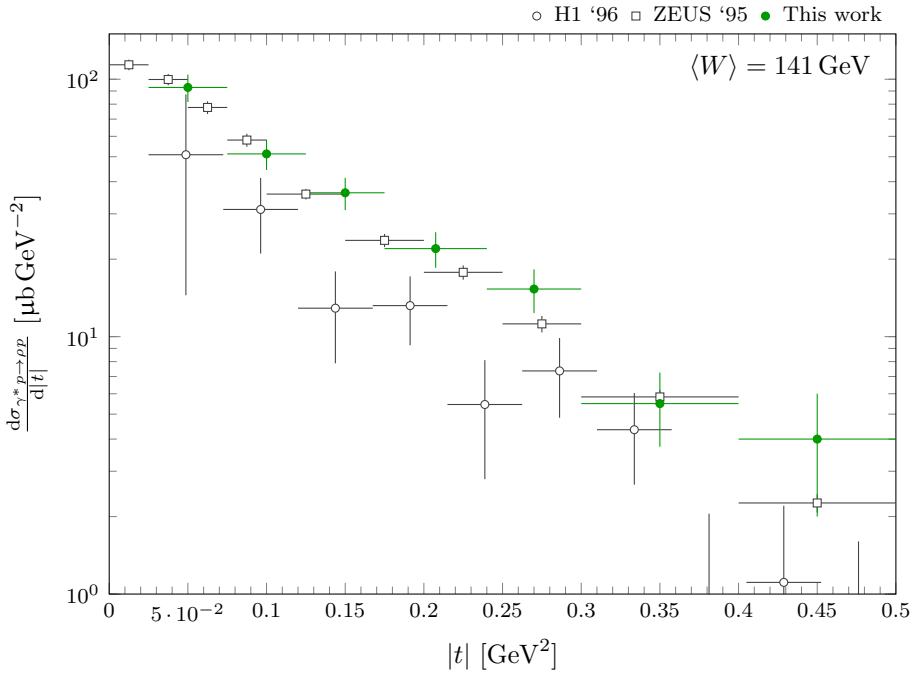

Figure 4.13: Comparison of our measurement of $\frac{\mathrm{d}\sigma_{\gamma p \to \rho p}}{\mathrm{d}|t|}$ with the results of past experiments.

Conclusions

In this work, we studied exclusive ρ^0 production in CMS 2013 proton-lead and lead-proton data at $\sqrt{s_{NN}} = 5.02\,\text{TeV}$, corresponding to a total integrated luminosity of $16.94\,\mu\text{b}^{-1}$. The first part of our work consisted in the selection of the event candidates and a study of exclusivity criteria using the CMS detector. Most CMS subdetectors are used in our analysis. The second part consisted in the removal of the remaining backgrounds and the measure of the $\gamma p \to \rho p$ cross section. Our results for $20 < W < 250\,\text{GeV}$, $|t| < 0.5\,\text{GeV}^2$ are consistent with those of FSQ-16-007, though somewhat higher, and in good agreement with measurements conducted prior to ours.

We showed that the barrel of the electromagnetic calorimeter could be used as an exclusivity criterion. The authors of FSQ-16-007 had found the converse, but their study was dominated by signal coming from "hot towers". Ignoring them and taking the nature of the noise into account makes it possible to define a cut. We found that the signal observed above this cut was compatible with physical information, and used it to refine our event selection.

We conducted a similar study for the barrel of the hadronic calorimeter, in which hot cells were also present. We found that a pseudorapidity-dependent cut was needed, and used the cylindrical symmetry of the detector to define one. We found that it excluded a negligible amount of events, and concluded that HB wasn't useful to isolate an exclusive ρ sample.

In order to remove remaining backgrounds from our event sample, we fitted a sum of signal and background templates to the p_t distribution. We found no evidence for a ρ' contribution distinct from the background templates. We showed that two templates could be used to describe the proton-dissociative background and lead to different (though mutually compatible) results. We made use of this information to estimate the systematic uncertainty associated to the chosen background templates. This systematics increases dramatically at high $|t|$: any result above $|t| \sim 0.2\,\text{GeV}^2$ has to take it into account, and it makes it very difficult to measure the t-differential cross section above $|t| \sim 0.5\,\text{GeV}^2$.

This being considered, we measured the W dependence of the exclusive $\gamma p \to \rho p$ cross section in the range $20 < W < 250\,\text{GeV}$ and the t-differential cross section for $0.025 < |t| < 0.5\,\text{GeV}^2$. Our results are compatible with measurements performed by the H1 [14] and ZEUS [15] collaborations. We found no diffractive dip in the t-differential cross section.

This work tends to develop a methodology for exclusive vector meson production in CMS. Future measurements of other exclusive processes, such as J/ψ or Υ photoproduction, are expected to be performed, in particular using

the large proton-lead data sample taken in 2016 at $\sqrt{s_{NN}} = 8\,\text{TeV}$. They would benefit from our work on exclusivity cuts. Since their production can be described in terms of the gluon PDFs or GPDs, measurements of the cross sections for these heavy vector mesons would directly constrain the low-x gluon density.

List of Figures

List of Tables

Bibliography

[1] The CMS Collaboration. Exclusive $\rho(770)$ photoproduction in ultra-peripheral pPb collisions at 5.02TeV. To be published.

[2] Schwartz, M. D. *The quantum theory of fields and the standard model* (Cambridge University Press, 2014).

[3] Burgard, C. Standard model of physics (2016). URL `http://www.texample.net/tikz/examples/model-physics`. Last viewed on May 14, 2017.

[4] Patrignani, C. *et al.* Review of particle physics. *Chin. Phys. C* **40**, 100001 (2016).

[5] Frère, J.-M. Physics beyond the standard model. Lectures at ULB (2016).

[6] Burkardt, M. & Pasquini, B. Modelling the nucleon structure. *Eur. Phys. J. A* 161 (2016).

[7] Favart, L. Physique auprès des collisionneurs. Lectures at ULB (2016).

[8] Bacchetta, A. Where do we stand with a 3-D picture of the proton? *Eur. Phys. J. A* **52**, 163 (2016).

[9] Kumerički, K., Liuti, S. & Moutarde, H. GPD phenomenology and DVCS fitting. *Eur. Phys. J. A* **52**, 157 (2016).

[10] Favart, L., Guidal, M., Horn, T. & Kroll, P. Deeply virtual meson production on the nucleon. *Eur. Phys. J A* **52**, 158 (2016).

[11] Léonard, A. *Production diffractive de mésons ρ à HERA II* . Master's thesis, ULB (2011).

[12] Kowalski, H., Motyka, L. & Watt, G. Exclusive diffractive processes at HERA within the dipole picture. *Phys. Rev. D* **74**, 074016 (2006).

[13] Armesto, N. & Rezaeian, A. H. Exclusive vector meson production at high energies and gluon saturation. *Phys. Rev. D* **90**, 054003 (2014).

[14] Aid, S. Elastic Photoproduction of ρ^0 Mesons at HERA. *Nucl. Phys. B* **463**, 3 (1996).

[15] The ZEUS Collaboration. Measurement of Elastic ρ^0 Photoproduction at HERA. *Z. Phys. C* **69**, 39–54 (1995).

[16] STAR Collaboration. Coherent diffractive photoproduction of ρ^0 mesons on gold nuclei at RHIC (2017). URL `http://arxiv.org/abs/1702.07705v1`. To be published in journal.

[17] The H1 Collaboration. Diffractive Electroproduction of ρ and ϕ Mesons at HERA. *JHEP* **05**, 032 (2010).

[18] ZEUS Collaboration. Exclusive ρ^0 production in deep inelastic scattering at HERA. *PMC Phys. A* **163**, 6 (2007).

[19] Henneaux, M. Gravitation avancée et théories des cordes. Lectures at ULB (2017).

[20] Klein, S. R., Nystrand, J., Seger, J., Gorbunov, Y. & Butterworth, J. STARlight: A Monte Carlo simulation program for ultra-peripheral collisions of relativistic ions. *Comput. Phys. Commun.* **212**, 258–268 (2017).

[21] CERN accelerator website (2015). URL `http://te-dep-epc.web.cern.ch`. Quoted in: Postiau, N. *Étude de la production de paires de bosons Z à grande masse invariante dans des collisions proton-proton à* $\sqrt{s} = 8\,\text{TeV}$ *auprès de l'expérience CMS*. Master's thesis, ULB (2015).

[22] The CMS Collaboration. The CMS experiment at the CERN LHC. *J. Inst.* **3**, S08004 (2008).

[23] Frühwirth, R. Application of Kalman filtering to track and vertex fitting. *Nucl. Instrum. Meth. A* **262**, 444–450 (1987).

[24] Druzhkin, D. Forward zone and CASTOR (2012). URL `https://twiki.cern.ch/twiki/pub/CMS/CastorDrawings/Forward_zone_CASTOR_Model_1.pdf`. Last viewed on May 2, 2017.

[25] CMS collaboration. Luminosity calibration for the 2013 proton-lead and proton-proton data taking. CMS PAS LUM-13-002 (2014).

[26] D'Agostini, G. A Multidimensional unfolding method based on Bayes' theorem. *Nucl. Instrum. Meth.* **A362**, 487–498 (1995).

[27] Adye, T. Unfolding algorithms and tests using RooUnfold. In *Proceedings of the PHYSTAT 2011 Workshop*, 313–318 (CERN, 2011).